This work was written as part of one of the author's official duties as an Employee of the United States Government and is therefore a work of the United States Government. In accordance with 17 U.S.C. 105, no copyright protection is available for such works under U.S. Law. Access to this work was provided by the University of Maryland, Baltimore County (UMBC) ScholarWorks@UMBC digital repository on the Maryland Shared Open Access (MD-SOAR) platform.

Please provide feedback

Please support the ScholarWorks@UMBC repository by emailing scholarworks-group@umbc.edu and telling us what having access to this work means to you and why it’s important to you. Thank you.

Draft version December 2, 2020
Typeset using LaTeX twocolumn style in AASTeX63

arXiv:2012.00160v1 [astro-ph.HE] 30 Nov 2020

A Comprehensive X-ray Report on AT2019wey

Yuhan Yao,[1] S. R. Kulkarni,[1] K. C. Gendreau,[2] Gaurava K. Jaisawal,[3] Teruaki Enoto,[4] Brian W. Grefenstette,[1] Herman L. Marshall,[5] Javier A. García,[1,6] R. M. Ludlam,[1,*] Sean N. Pike,[1] Mason Ng,[5] Liang Zhang,[7] Diego Altamirano,[7] Amruta Jaodand,[1] S. Bradley Cenko,[8] Ronald A. Remillard,[5] James F. Steiner,[9] Hitoshi Negoro,[10] Murray Brightman,[1] Amy Lien,[11,12] Michael T. Wolff,[13] Paul S. Ray,[13] Koji Mukai,[14,12] Zorawar Wadiasingh,[8,15] Zaven Arzoumanian,[8] Nobuyki Kawai,[16] Tatehiro Mihara,[17] and Tod E. Strohmayer[8]

[1] *Cahill Center for Astronomy and Astrophysics, California Institute of Technology, Pasadena, CA 91125, USA*
[2] *Mail Code 662.1, Goddard Space Flight Center, Greenbelt, MD 20771, USA*
[3] *National Space Institute, Technical University of Denmark, Elektrovej 327-328, DK-2800 Lyngby, Denmark*
[4] *Extreme Natural Phenomena RIKEN Hakubi Research Team, Cluster for Pioneering Research, RIKEN, 2-1 Hirosawa, Wako, Saitama 351-0198, Japan*
[5] *MIT Kavli Institute for Astrophysics and Space Research, 70 Vassar Street, Cambridge, MA 02139, USA*
[6] *Dr. Karl Remeis-Observatory and Erlangen Centre for Astroparticle Physics, Sternwartstr. 7, 96049 Bamberg, Germany*
[7] *Department of Physics and Astronomy, University of Southampton, Southampton, SO17 1BJ, UK*
[8] *Astrophysics Science Division, NASA Goddard Space Flight Center, Greenbelt, MD 20771, USA*
[9] *Harvard-Smithsonian Center for Astrophysics, 60 Garden St., Cambridge, MA 02138, USA*
[10] *Department of Physics, Nihon University, 1-8, Kanda-Surugadai, Chiyoda-ku, Tokyo 101-8308*
[11] *Center for Research and Exploration in Space Science and Technology (CRESST) and NASA Goddard Space Flight Center, Greenbelt, MD 20771, USA*
[12] *Department of Physics, University of Maryland, Baltimore County, 1000 Hilltop Circle, Baltimore, MD 21250, USA*
[13] *Space Science Division, U.S. Naval Research Laboratory, Washington, DC 20375, USA*
[14] *CRESST II and X-ray Astrophysics Laboratory, NASA/GSFC, Greenbelt, MD 20771, USA*
[15] *Universities Space Research Association (USRA), Columbia, MD 21046, USA*
[16] *Department of Physics, Tokyo Institute of Technology, 2-12-1 Ookayama, Meguro-ku, Tokyo 152-8551*
[17] *Cosmic Radiation Laboratory, RIKEN, 2-1 Hirosawa, Wako, Saitama 351–198*

Abstract

The Galactic low-mass X-ray binary AT2019wey (ATLAS19bcxp, SRGA J043520.9+552226, SRGE J043523.3+552234, ZTF19acwrvzk) was discovered as a new optical transient in Dec 2019, and independently as an X-ray transient in Mar 2020. In this paper, we present comprehensive *NICER*, *NuSTAR*, *Chandra*, *Swift*, and *MAXI* observations of AT2019wey from $\sim$1 year prior to the discovery to the end of September 2020. AT2019wey appeared as a $\sim$1 mCrab source and stayed at this flux density for several months, displaying a hard X-ray spectrum that can be modeled as a power-law with photon index $\Gamma \sim 1.8$. In June 2020 it started to brighten, and reached $\sim$20 mCrab in $\sim$2 months. The inclination of this system can be constrained to $i \lesssim 30^\circ$ by modelling the reflection spectrum. Starting from late-August ($\sim$59082 MJD), AT2019wey entered into the hard-intermediate state (HIMS), and underwent a few week-long timescale outbursts, where the brightening in soft X-rays is correlated with the enhancement of a thermal component. Low-frequency quasi-periodic oscillation (QPO) was observed in the HIMS. We detect no pulsation and in timing analysis of the *NICER* and *NuSTAR* data. The X-ray states and power spectra of AT2019wey are discussed against the landscape of low-mass X-ray binaries.

Keywords: X-rays: individual (AT2019wey) – accretion, accretion disks – black hole physics

1. Introduction

AT2019wey, though discovered as an optical transient by the ATLAS (Tonry et al. 2018) optical survey in December 2019 (Tonry et al. 2019), only rose to prominence with the discovery of strong X-ray emis-

yyao@astro.caltech.edu

* NASA Einstein Fellow

sion by the eROSITA (Merloni et al. 2012; Predehl et al. 2020) and the Mikhail Pavlinsky ART-XC (Pavlinsky et al. 2018) telescopes on board the *Spektrum-Roentgen-Gamma* (*SRG*) satellite in mid March 2020. Upon detection, the X-ray flux was 0.36 mCrab in the 0.3–8 keV band and 0.59 mCrab in the 4–12 keV band (Mereminskiy et al. 2020). No significant variability was detected between four ART-XC consecutive passages separated by 4 hour intervals. We note that there is no point source detected at the position of AT2019wey in the 2nd *ROSAT* All-Sky Survey Point Source Catalog (2RXS; Boller et al. 2016), providing a historical X-ray upper limit of $\sim 10\,\mu$Crab.

Initially AT2019wey was thought to be a supernova (Mereminskiy et al. 2020) and subsequently proposed to be a BL Lac object (Lyapin et al. 2020). Yao et al. (2020b) reported the detection of hydrogen lines at redshift $z = 0$, and proposed AT2019wey to be a Galactic accreting binary. In this paper, we show that the timing and spectral X-ray properties of AT2019wey are consistent with low-mass X-ray binaries (LMXBs) with a black hole (BH) or neutron star (NS) accretor. Based on this conclusion, we derive upper limits from historical optical and radio surveys and investigate the multi-wavelength evolution of this source in Yao et al. (2020, hereafter Paper II), from which we infer that the central object is probably a BH, and that the orbital period of this system is short ($P_{\rm orb} \lesssim 8$ hours).

The comprehensive X-ray observations of AT2019wey presented in this paper spans from pre-discovery to 30 September 2020. The data are obtained using the *Neutron Star Interior Composition Explorer* (*NICER*; Gendreau et al. 2016), the Nuclear Spectroscopic Telescope ARray (*NuSTAR*; Harrison et al. 2013), the *Chandra* X-ray Observatory (CXO; Wilkes & Tucker 2019), the *Neil Gehrels Swift Observatory* (Gehrels et al. 2004), and the Monitor of All-sky X-ray Image (*MAXI*) mission (Matsuoka et al. 2009). As of the time of submission of the paper (November 2020), the source is still active.

The paper is organized as follows. In Section 2 we summarize the X-ray observations. In Section 3 and Section 4 we report the timing analysis using *NICER* and *NuSTAR* data, respectively. We present joint spectroscopic analysis in Section 5. In Section 6 we provide an investigation of spectral evolution using *NICER* data. We conclude in Section 7.

2. Observations

2.1. NICER Observation

AT2019wey was observed by the X-ray Timing Instrument (XTI) on board *NICER* beginning on 04 August 2020 (PI: K. Gendreau; Table 1). *NICER* is a soft X-ray telescope on board the International Space Station (ISS). It was launched in 2017 June. *NICER* is comprised of 56 co-aligned concentrator X-ray optics, each paired with a single-pixel silicon drift detector. Presently, 52 detectors are active with a peak effective area of ~ 1900 cm^2 at 1.5 keV, and 50 of these were selected (excluding modules 14 and 34) to make the light curves reported in this paper. The *NICER* observations were processed using HEASOFT version 6.27 and the *NICER* Data Analysis Software (NICERDAS) version 7.0 (2020-04-23_V007a). We used the latest calibration files obtained from the standard CALDB release for *NICER*, downloaded from NASA's High Energy Astrophysics Science Archive Research Center (HEASARC).

To generate a background-subtracted light curve, we first define good time intervals (GTIs) with as much data as possible. Then we compute background using the `nibackgen3C50` tool (Remillard et al. in prep). For each GTI, we explicitly subtract background-predicted spectrum from the raw extraction to get the source net spectrum. We also remove GTIs with $|hbg|$[1]> 0.07, to exclude GTIs with less accurate background subtraction. Finally, we compute count rate in five energy bands: 0.4–1.0 keV, 1–2 keV, 2–4 keV, 4–12 keV, and 0.4–12 keV.

The upper panel of Figure 1 shows that the X-ray brightening continues to about 330 count s^{-1} on Aug 21 (59082 MJD), after which the source underwent a few short term bumps, each lasting for about 1 week. At the end of September, the source count rate drops back to 330 count s^{-1}. The lower right panel of Figure 1 shows *NICER* hardness ratios. During the small outbursts, the hard color decreases and the soft color increases. Figure 2 presents the *NICER* hardness-intensity diagram (HID) of AT2019wey. The evolution of AT2019wey roughly follows a single line on the HID, i.e., each hardness value corresponds to a single value of count rate.

2.2. NuSTAR Observation

We obtained three epochs of Target of Opportunity (ToO) observations using the hard X-ray telescope *NuSTAR* (PI: Y. Yao, Table 2). In this paper, we report the analysis for the first two sequences (sequence IDs 90601315002 and 90601315004, hereafter 002 and 004, respectively). In Tao et al. (in prep) we report the third epoch, which was carried out jointly with the Hard X-ray Modulation Telescope (HXMT; Zhang et al. 2020b).

[1] *hbg* is the count rate in the 13–15 keV band, which is beyond the effective area of the concentrator optics, as defined in Remillard et al. 2020).

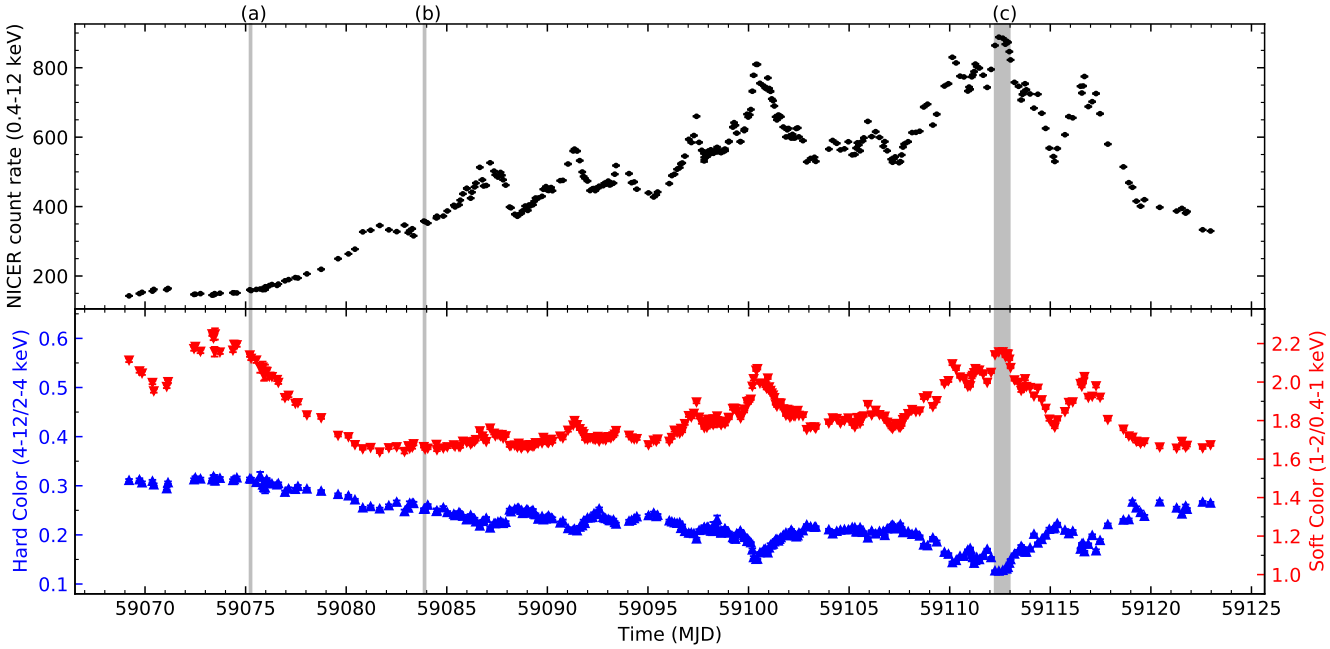

Figure 1. *Upper*: *NICER* (0.4–12 keV) light curve of AT2019wey. *Bottom*: *NICER* hard color (ratio of the 4–12 keV and 2–4 keV count rates) of AT2019wey is shown in blue (upward triangles) and soft color (ratio of the 1–2 keV and 0.4–1 keV count rates) is shown in red (downward triangles). Note that 59070 MJD is 09 Aug 2020. The three vertical grey regions mark epochs where detailed timing analysis are performed (see Section 3.1 and Table 4.)

Table 1. *NICER* Observation Log

OBSID	Exp. (ks)	Start Time (UT)	OBSID	Exp. (ks)	Start Time (UT)	OBSID	Exp. (ks)	Start Time (UT)
3201710105	0.22	2020-08-09 08:28	3201710106	1.10	2020-08-10 01:30	3201710107	4.82	2020-08-11 09:59
3201710108	6.02	2020-08-12 07:43	3201710109	4.39	2020-08-13 08:30	3201710110	8.00	2020-08-14 04:38
3201710111	10.55	2020-08-15 00:54	3201710112	4.21	2020-08-16 03:01	3201710113	4.85	2020-08-17 00:43
3201710114	2.52	2020-08-18 13:52	3201710115	7.41	2020-08-19 02:14	3201710116	3.15	2020-08-20 04:51
3201710117	2.32	2020-08-21 02:37	3201710118	6.39	2020-08-22 02:07	3201710119	3.57	2020-08-23 00:59
3201710120	5.87	2020-08-24 00:25	3201710121	8.95	2020-08-24 23:36	3201710122	7.58	2020-08-26 03:29
3201710123	7.76	2020-08-27 02:43	3201710124	10.07	2020-08-28 00:25	3201710125	3.65	2020-08-29 01:12
3201710126	6.54	2020-08-30 00:26	3201710127	7.99	2020-08-31 02:49	3201710128	4.84	2020-09-01 00:31
3201710129	2.97	2020-09-02 01:18	3201710130	3.71	2020-09-03 00:31	3201710131	6.90	2020-09-04 01:18
3201710132	8.44	2020-09-05 00:32	3201710133	5.43	2020-09-06 02:46	3201710134	12.36	2020-09-07 00:05
3201710135	13.69	2020-09-08 01:08	3201710136	23.53	2020-09-09 00:29	3201710137	14.38	2020-09-10 01:13
3201710138	5.67	2020-09-11 01:47	3201710139	8.76	2020-09-11 23:34	3201710140	11.32	2020-09-13 03:34
3201710141	10.02	2020-09-14 02:35	3201710142	10.49	2020-09-15 02:07	3201710143	5.80	2020-09-16 02:51
3201710144	5.45	2020-09-17 03:40	3201710145	8.38	2020-09-18 02:58	3201710146	10.22	2020-09-19 00:12
3201710147	16.59	2020-09-20 01:03	3201710148	6.54	2020-09-21 00:13	3201710149	11.19	2020-09-21 23:27
3201710150	8.84	2020-09-23 03:24	3201710151	5.97	2020-09-24 01:02	3201710152	3.34	2020-09-25 01:52
3201710153	3.82	2020-09-26 01:06	3201710154	2.53	2020-09-27 01:52	3201710155	3.11	2020-09-28 01:06
3201710156	4.25	2020-09-29 00:20	3201710157	6.22	2020-09-30 01:10			

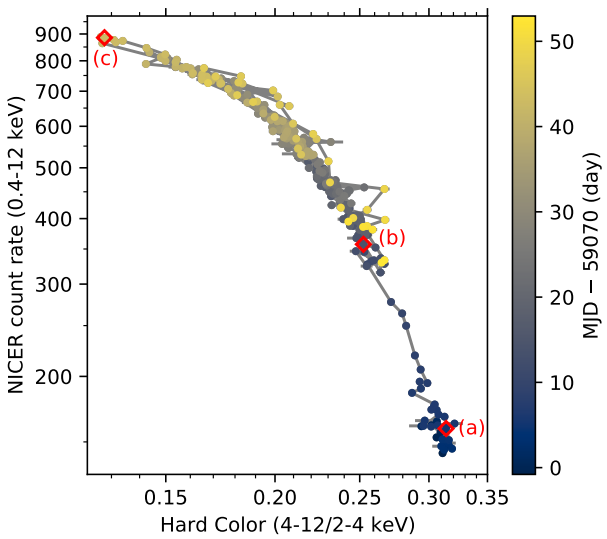

Figure 2. The *NICER* hardness–intensity diagram, defined as the 0.4–12 keV count rate versus the hard color. The data points are color coded by time. The three red diamonds mark epochs where detailed timing analysis are performed (see Section 3.1 and Table 4).

Table 2. *NuSTAR* Observation Log

OBSID	Exp. (ks)	Start Time (UT)	Count Rate (s^{-1})
90601315002	38	2020-04-18 11:21	2.3 ± 0.7
90601315004	42	2020-08-16 12:16	30.8 ± 2.6
90601315006	37	2020-08-27 02:51	35.1 ± 2.7

The focal plane of *NuSTAR* consists of two photon counting detector modules (FPMA and FPMB). The data were processed using the *NuSTAR* Data Analysis Software (NUSTARDAS) v2.0.0 along with the 2020423 *NuSTAR* CALDB using the default data processing parameters.

2.3. *Chandra Observation*

We requested and were granted 25 ks of *Chandra* director's discretionary time (PI: S. R. Kulkarni; OBSID = 24651) to obtain a high-energy transmission grating spectrometer (HETGS; Markert et al. 1994; Canizares et al. 2005) spectrum using the Advanced CCD Imaging Spectrometer (ACIS; Garmire et al. 2003). The black arrow in the top panel of Figure 1 marks the epoch of *Chandra* observation, which was carried out in the timed event (TE) mode around the maximum soft X-ray luminosity of AT2019wey. During the exposure (from 2020-09-20T17:43 to 2020-09-21T01:12), the source count rate varies between 23.1 count s^{-1} to 24.5 count s^{-1}.

The HETGS spectrometer is composed of two sets of gratings (see, e.g., Chapter 2 of Wilkes & Tucker 2019): the medium-energy gratings (MEGs), covering the 0.4–7 keV energy band and the high-energy gratings (HEGs) in the 0.8–10.0 keV band. No strong narrow emission or absorption lines were detected in the HETGS spectrum. A detailed modeling of the *Chandra* spectrum is presented in Section 5.2.3.

2.4. *MAXI Observation*

MAXI was installed on the Japanese Experiment Module Exposed Facility on the ISS on 23 July 2009. Since 15 August 2009, the *MAXI* Gas Slit Cameras (GSCs; Mihara et al. 2011; Sugizaki et al. 2011), with very wide fields-of-views have been observing the source region of AT2019wey in the 2–20 keV band every 92 min synchronized with the ISS orbital period.

Due to the ISS orbit precession of about 72 days, the source region, due to the interference of some structure of the detectors, is regularly unobservable for about 12 days. Furthermore, in recent years, the source is only observed with the degraded cameras for $\sim$ 28 days in each precession period. We do not use these data. As a result, there are two data gaps every 72 days.

The 1-day average *MAXI* X-ray light curves are generated by the point-spread-function fit method (Morii et al. 2016) to obtain the most reliable curves in the 2–4 keV and 4–10 keV bands. Furthermore, we exclude data with 1-σ uncertainties 2.5 times larger than the average uncertainties in the 2–4 and 4–10 keV bands, respectively. Then, we rebin the data into 4 day bins to improve the statistics. The *MAXI* light curve is shown in the top two panels of Figure 3.

The GSC data show no significant count excess before the optical discovery (also see Hori et al. 2018). The GSC, however, detected a significant count excess (1.7 ± 0.4 mCrab) after the optical detection (see Negoro et al. 2020); see Figure 3.

2.5. *Swift Observation*

2.5.1. *XRT*

AT2019wey was observed by the X-Ray Telescope (XRT; Burrows et al. 2005) on board the *Neil Gehrels Swift Observatory* (Gehrels et al. 2004) starting 12 April 2020. We generated the X-ray light curve for AT2019wey using the automated online tools available at https://www.swift.ac.uk/user_objects (see Evans et al. 2007, 2009 for details). The first 9 epochs were obtained in Photon Counting (PC) mode, and thus suffer from "pile-up" at the high observed count rates. Stan-

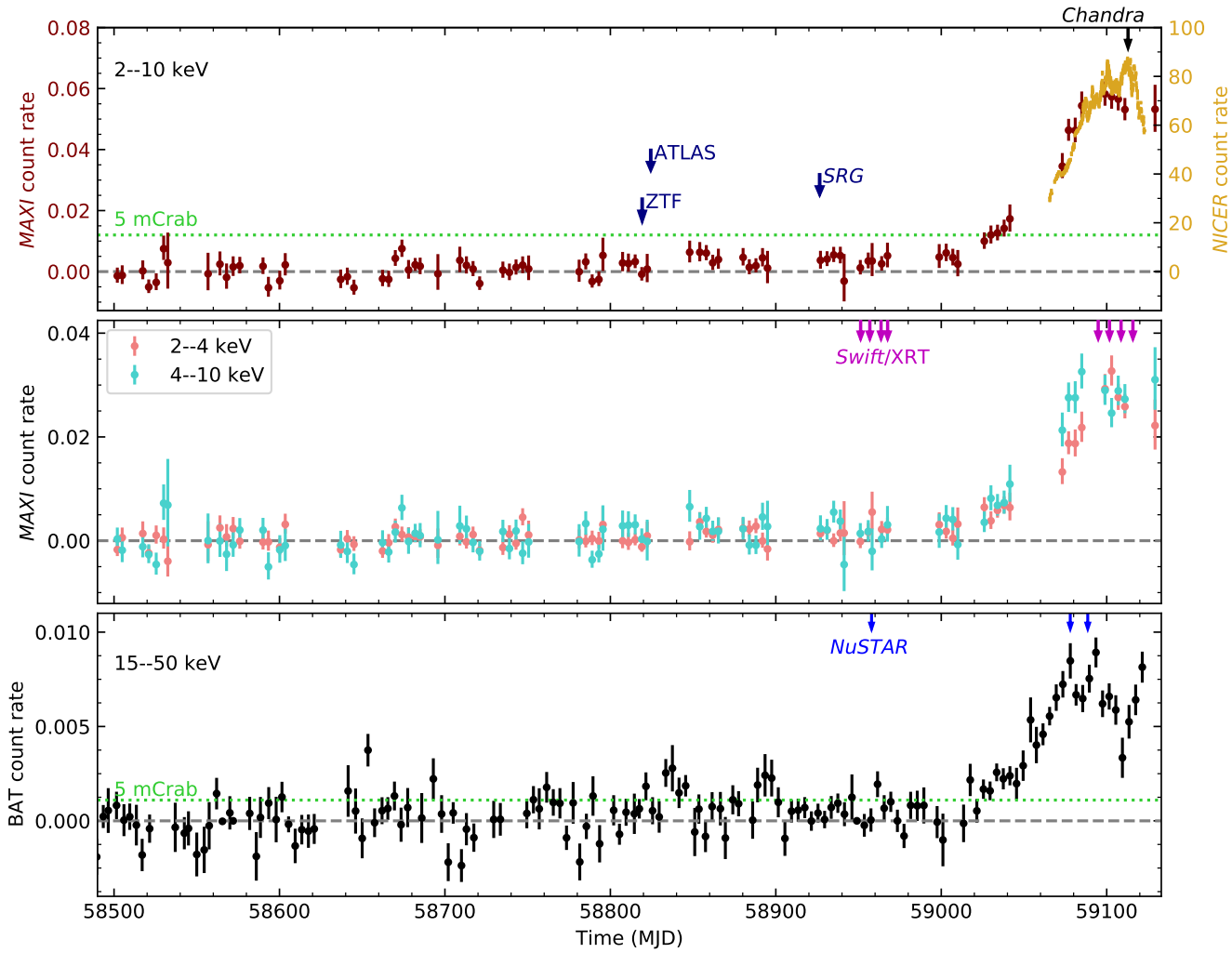

Figure 3. *Upper*: *NICER* and *MAXI* light curves of AT2019wey in 2–10 keV. The three dark blue arrows mark epochs of the Zwicky Transient Facility (ZTF; Bellm et al. 2019; Graham et al. 2019) first detection (see Paper II), ATLAS discovery, and *SRG* discovery. The black arrow marks the epoch of *Chandra* observation. *Middle*: *MAXI* light curves in 2–4 keV and 4–10 keV. The magenta arrows along the top axis mark epochs of *Swift*/XRT observations (Table 3). *Bottom*: *Swift*/BAT light curve (count $\mathrm{cm}^{-2}\,\mathrm{s}^{-1}$) of AT2019wey in 15–50 keV. The three blue arrows along the top axis mark epochs of *NuSTAR* observations (Table 2).

dard corrections (Evans et al. 2007) were applied to the observations taken in April 2020. The observations from August 2020 were sufficiently piled up that no reliable count rates could be obtained. Beginning in September 2020, XRT observations were obtained in Window Timing (WT) mode, where larger count rates can still be reliably measured. The resulting count rate measurements are shown in Table 3.

We fit the spectrum of AT2019wey at two epochs: the PC mode data taken in April 2020, and the WT mode data taken in September 2020. In both cases we assumed a power-law (PL) spectrum with photon index Γ and fixed the column density to the Galactic value of $5.0 \times 10^{21}\,\mathrm{cm}^{-2}$ (Willingale et al. 2013). For the PC mode observations in April 2020 we find $\Gamma = 1.54 \pm 0.11$, while for the WT mode observations undertaken in September 2020 we find Γ increases from ~ 3.1 to ~ 3.5. We convert the count rates to 0.3–10.0 keV unabsorbed flux measurements, with the results reported in Table 3. Note that a simple power-law model is not enough to describe the WT mode observations obtained in September. A careful spectral fitting is presented in Section 6.

2.5.2. BAT

AT2019wey has been monitored by the Burst Alert Telescope (BAT; Krimm et al. 2013) on-board *Swift*. We show the *Swift*/BAT transient monitor results pro-

Table 3. *Swift* XRT Observations of AT2019wey

OBSID	Exp. (s)	Start Time (UT)	Mode	Count Rate (s^{-1})	Unabsorbed Flux (10^{-11} erg cm^{-2} s^{-1})
13313001	1523	2020-04-12 06:07	PC	0.645 ± 0.029	4.84 ± 0.22
13313002	874	2020-04-17 19:55	PC	0.570 ± 0.035	4.27 ± 0.26
13313003	1026	2020-04-24 14:28	PC	0.639 ± 0.036	4.79 ± 0.27
13313004	1043	2020-04-28 13:56	PC	0.717 ± 0.051	5.38 ± 0.38
13313010	434	2020-09-02 20:36	WT	$27.57^{+0.28}_{-0.31}$	$325.9^{+12.5}_{-12.0}$
13313011	1023	2020-09-09 16:40	WT	$42.50^{+1.58}_{-1.54}$	$660.8^{+13.3}_{-13.1}$
13313012	858	2020-09-16 16:01	WT	$43.32^{+0.26}_{-0.29}$	$652.3^{+56.0}_{-50.8}$
13313013	794	2020-09-23 20:03	WT	$40.53^{+2.35}_{-2.27}$	$789.2^{+18.6}_{-18.2}$

Note—Count rate and unabsorbed flux are given in the 0.3–10 keV band.

vided by the Swift/BAT team[2] in the bottom panel of Figure 3. We exclude data with 1-σ uncertainties 3 times larger than the median uncertainties, and rebin the data into 4-day bins to improve the statistics.

The *MAXI* and BAT light curves demonstrate that there was no strong X-ray nova outburst around the optical discovery epoch. A comparison between the top and bottom panels of Figure 3 shows that after the X-ray brightening around $\sim$ 59070 MJD, AT2019wey underwent a few outbursts in the *NICER* 2–10 keV band, but stays roughly constant in the BAT 15–50 keV band.

3. *NICER* Timing Analysis

NICER/XTI provides light curve in the 0.2–12 keV energy band with an unprecedented timing precision of $\sim$ 100 ns, making it an ideal instrument to study fast X-ray variability. Here we present aperiodic analysis (Section 3.1) and pulsation search (Section 3.2) using *NICER* data.

3.1. Aperiodic Analysis

To study the X-ray variability, we produced an average Power Density Spectrum (PDS) in the 0.5–12 keV energy band for each GTI. We used 16-s long intervals and 8192^{-1} s time resolution, so that the Nyquist frequency is 4096 Hz. The average PDS were rms-normalized (Belloni & Hasinger 1990) and the contribution due to the photon counting noise was subtracted. We calculated the integrated fractional rms in the 0.1–64 Hz frequency range. We also calculated the absolute rms by multiplying the fractional rms by the net count rate (Muñoz-Darias et al. 2011).

In Figure 4 we show the hardness-fractional rms diagram (HRD). The integrated fractional rms generally decreased from $\sim$30% to $\sim$10% as the spectra softened. In Figure 5 we show the absolute rms-intensity diagram (RID). At the beginning of the outburst, we found that the abosulte rms increases with the count rate. This linear trend has been observed in many BH binaries, and is commonly known as the 'hard line' (HL, Muñoz-Darias et al. 2011). Starting from $\sim$59082 MJD, the source left the HL and moved upwards. During the bumps observed between $\sim$59098 and $\sim$59123 MJD, the source moved to the left as the count rate increases, and then went back as the count rate decreases.

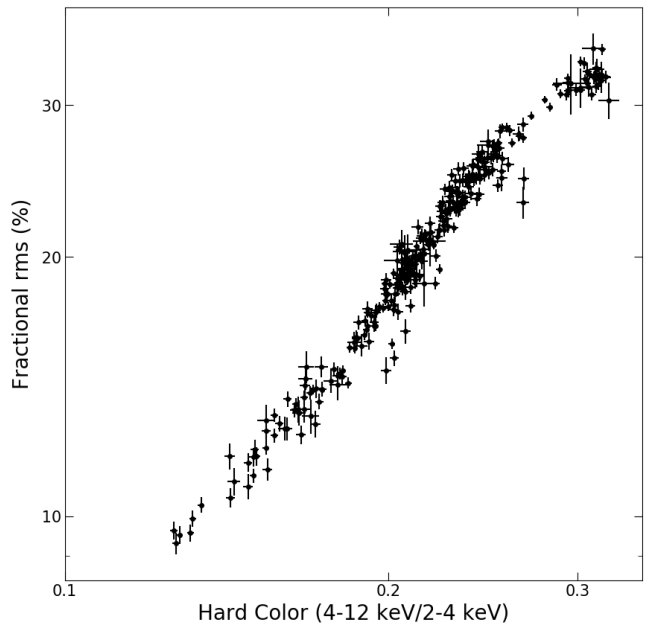

Figure 4. *NICER* hardness–fractional rms diagram (HRD). The integrated fractional rms was calculated in the 0.1–64 Hz frequency range.

During the period we analyzed, the PDS can be well fitted with two or three Lorentzian functions following the prescription laid out by Belloni et al. (2002).

[2] See the BAT scaled map data at https://swift.gsfc.nasa.gov/results/transients/weak/AT2019wey/.

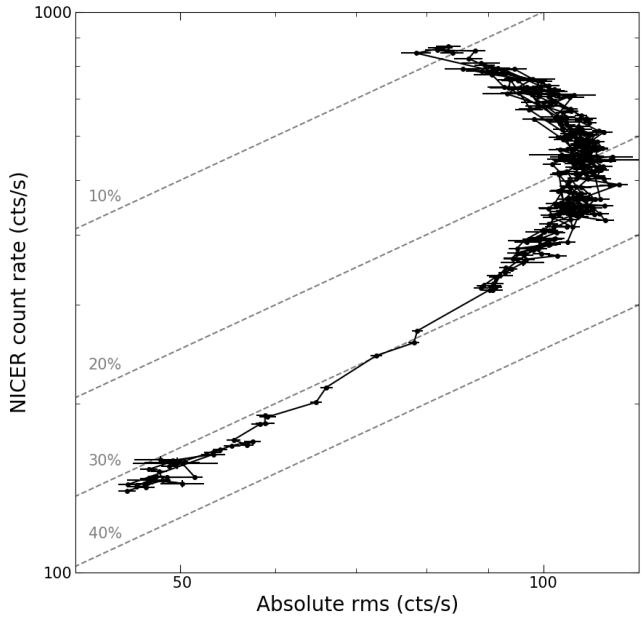

Figure 5. *NICER* absolute rms versus intensity diagram (RID). The absolute rms was calculated by multiplying the fractional rms (0.1–64 Hz) by the net count rate. The gray dotted lines represent the 10, 20, 30 and 40 percent fractional rms levels.

In Figure 6 we show three representative PDS averaged from different phases of the outburst (marked as grey regions in Figure 1 and red diamonds in Figure 2).

Table 4. *NICER* power spectral components

TIME (MJD)		$\nu_{\max}$ (Hz)	Q	rms (%)
59075.20–59075.29	L_1	0.33 ± 0.02	0.25 ± 0.08	27.57 ± 1.12
	L_2	1.76 ± 0.14	0.44 ± 0.12	16.33 ± 1.62
59083.85–59083.94	L_1	0.59 ± 0.02	0.26 ± 0.04	24.62 ± 0.34
	L_2	2.06 ± 0.03	6 (fixed)	3.95 ± 0.41
	L_3	3.53 ± 0.16	0.81 ± 0.14	10.17 ± 0.69
59112.24–59112.98	L_1	2.21 ± 0.03	0.34 ± 0.02	9.72 ± 0.07
	L_2	6.58 ± 0.21	4.99 ± 1.97	1.64 ± 0.26

The main properties of the PDS are listed in Table 4. At the beginning of the outburst, the PDS were dominated by strong band-limited noise without showing any significant QPOs. The average PDS can be fitted with two broad Lorentzians (Figure 6a). Starting from ∼59083 MJD, a weak QPO was sometimes observed in the PDS. The characteristic frequency of the QPO increased from ∼2 Hz to ∼ 6.5 Hz as the spectra softened. Based on the properties of the QPO and noise, this QPO is similar to the type-C QPO (e.g. Casella et al. 2005; Motta et al. 2011; Ingram & Motta 2019; Zhang et al. 2020a) commonly observed in BH and NS binaries (see, e.g., Klein-Wolt & van der Klis 2008).

3.2. Pulsation Search

Pulsation searches were carried out for data up to 2020 September 30. This includes 2257 GTIs and 394 ks of data. Upon cursory inspection of the data with `NICERsoft`[3], we found that detectors 34 and 43 suffered from high optical loading, thus the events in these detectors were removed from the event file. The events were barycentered using RA = 68.84698°, DEC = +55.37619° (equinox J2000.0), and with the JPL-DE405 solar system ephemeris using `barycorr` in `FTOOLS`. We employed acceleration search and stacked power spectral search schemes to search for pulsations. This is elaborated upon in Section 3.2.1 and 3.2.2.

3.2.1. Acceleration Searches

To account for possible frequency shifts due to binary Doppler motion, we employed an acceleration search algorithm over the f-$\dot{f}$ plane in the open source `PRESTO` pulsar timing software[4]. The acceleration search is valid under the assumption that the pulsar has a constant acceleration throughout the observation, and is most effective for observation durations $T \lesssim P_{\rm orb}/10$ (Ransom et al. 2002), where $P_{\rm orb}$ is the binary period.

To determine the GTIs (and hence event files) used in the acceleration searches, we started from the 2257 GTIs in the original filtered event file described above. Adjacent GTIs that were less than 11 seconds apart were combined, in order to prevent very short GTIs from being used in the searches. This resulted in a total of 445 GTIs, ranging in length from 1 s to 2648 s. We impose a minimum GTI duration of 64 s to avoid spurious signals in short GTIs, leaving us with 378 GTIs, with a median length of 883 s. For each of these GTIs (considered independently), we further filtered events from three energy ranges: 0.5–2 keV, 2–12 keV, and 0.5–12 keV. The 1134 event files were then extracted with `niextract-events`. We then ran the search using the `accelsearch` task in `PRESTO` over the range 1–1000 Hz, positing that Doppler shifting would cause the possible signal to drift across a maximum of 100 Fourier frequency bins, which for the median GTI length (883 s) and a fiducial fundamental pulsation frequency of 300 Hz, corresponds to accelerations up to $a = z_{\max}c/(fT^2) \approx 130\,{\rm m\,s^{-2}}$. The typical acceleration in a NS LXMB, say in a 12-hour orbit around a $0.2M_\odot$ companion, is approximately $5.7\,{\rm m\,s^{-2}}$.

[3] https://github.com/paulray/NICERsoft

[4] https://github.com/scottransom/presto

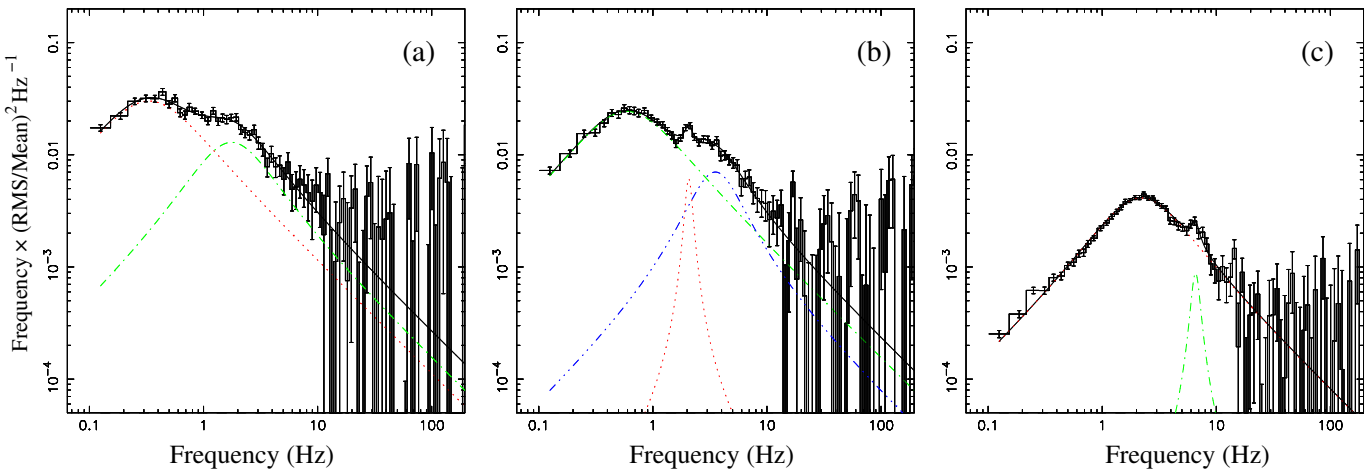

Figure 6. Representative *NICER* power spectra. The power spectra were calculated in the 0.5–12 keV energy band. The main properties of the power spectra are listed in Table 4. Panels b and c show the PDS of the QPO with the lowest and highest frequency, respectively.

The acceleration searches yielded no candidate signals above the statistical significance threshold of 3-σ, after accounting for the total number of trials.

3.2.2. *Stacked Power Spectral Searches*

An alternative pulsation search algorithm involves stacking power spectra from M segments and calculating an averaged power spectrum. This is Bartlett's method (Bartlett 1948), in which the original time series is broken up into M non-overlapping segments of equal length. The M segments are binned at $\Delta t = 0.5$ ms, such that we are sampling at the Nyquist frequency of 1000 Hz. The Leahy-normalized power spectrum is then computed, for each of the M segments, using the `realfft` task in `PRESTO` (Leahy et al. 1983). Finally, the M resulting spectra are averaged and the corresponding noise distributions are calculated. The detection level for any candidate signal is then determined by calculating the probability that the power in any frequency bin exceeds that of a detection threshold (say, 3σ), and this is calculated through the integrated probability of the χ^2 distribution with $2MW$ degrees of freedom, where W is the rebinning factor (van der Klis 1988). The stacking procedure is done to enhance the signal of faint millisecond pulsars. It reduces the variance of the noise-induced fluctuations, at the expense of coarser frequency resolution.

The stacked power spectra were calculated with segments of length 64, 128, 256, and 512 s, to account for possible orbital modulations in the pulsar frequency with yet unknown binary parameters. On top of stacking the power spectra from segments of the entire time series, the stacked power spectra were also calculated for various sub-time series, where the choices were informed by the overall light curve binned at 128 s and looking at the source brightness level (in count s^{-1}). The number of segments admitted into the calculation for the stacked power spectrum also depended on a segment threshold (in %); that is, for each segment, a 1-s binned light curve was generated, and if the fraction of bins with counts is less than the threshold, then that segment is not used in the calculation. Segment thresholds used were 20%, 50%, 70%, and 100%. We also searched over energy ranges 0.5–2 keV, 2–12 keV, and 0.5–12 keV. The averaged power spectrum is finally calculated by dividing the total power spectrum by the number of segments used.

From all of these stacked power spectra, there were no candidate signals that exceeded the 3-σ detection level, after accounting for the total number of trials.

4. *NuSTAR* Timing Analysis

4.1. *Aperiodic Analysis*

4.1.1. *Producing Cospectra*

Our starting point is the cleaned event list produced by `nupipeline`. We first corrected the photon arrival times for the position and motion of *NuSTAR*, moving the arrival times into the reference frame of the solar system barycenter. Next we filtered the events using source regions which were centered on the source centroid and which had radii of 60″ and 90″ for 002 and 004, respectively. We chose to use a larger source region for observation 004 due to its higher count rate. Finally, we filtered the events by energy, keeping only those events with photon energy between 3 and 78 keV. For each observation, we were thus left with two lists of filtered and barycenter corrected events – one for FPMA and one for FPMB. Using the X-ray timing package `Stingray` (Huppenkothen et al. 2019) we produced light curves

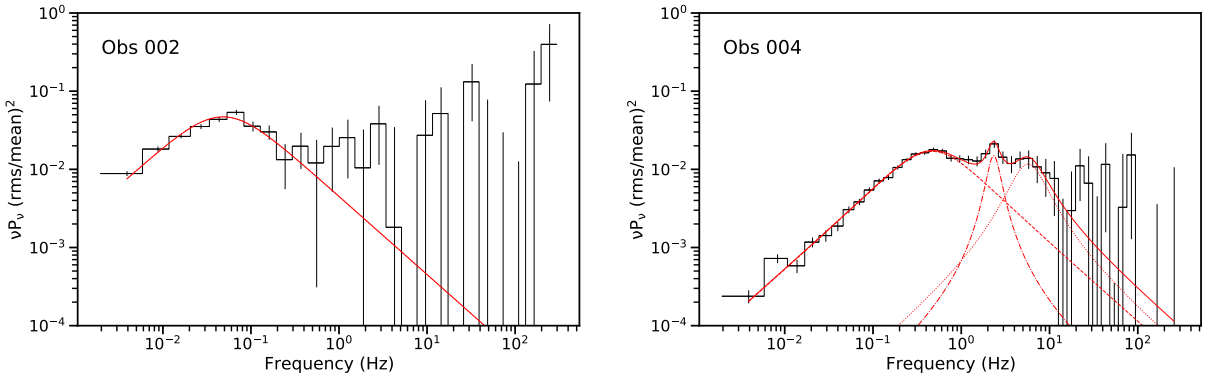

Figure 7. The averaged rms-normalized cospectra for each observation are shown in black in units of Power × Frequency, with observation 002 on the left and 004 on the right. Their best-fit models are plotted in solid red and the individual Lorentzian components, L_b, $L_{\rm LF}$, and L_h, are shown in dashed, dashed-dotted, and dotted red, respectively. Cospectra have been rebinned for legibility.

for each of these event lists. We binned the light curves with a time resolution of 512^{-1} s. `Stingray` automatically applied the GTIs recorded by the instrument.

Rather than summing the FPMA and FPMB light curves and producing PDS for each observation, we chose to analyze the Cross Power Density Spectrum (CPDS). The CPDS taken between FPMA and FPMB is given by

$$C(\nu) = \mathcal{F}_{\rm A}^{*}(\nu)\mathcal{F}_{\rm B}(\nu) \quad (1)$$

where $\mathcal{F}_{\rm A}^{*}(\nu)$ is the complex conjugate of the Fourier transform of the light curve observed by FPMA and $\mathcal{F}_{\rm B}(\nu)$ is the Fourier transform corresponding to FPMB.

The CPDS between two light curves gives the relationship between their variability properties. The real part of the CPDS, called the cospectrum, represents only the power of the signals which are in phase between the two light curves, and its imaginary part gives the power of those signals which are in quadrature. The CPDS can therefore be used to calculate time lags and correlations between two light curves. It is often used to compare the variability between different energy bands as measured by a single instrument. In addition, these properties make the CPDS particularly useful for analyzing *NuSTAR* data. Whereas the PDS requires careful noise subtraction to account for dead time and Poisson noise, the cospectrum calculated between FPMA and FPMB brings the average white noise level down to 0 since these effects are not correlated between the two instruments. For more information about the CPDS, the cospectrum, and its applications for *NuSTAR* timing analysis, see Bachetti et al. (2015).

In order to produce a cospectrum for each observation, we split the light curves observed by each FPM into intervals of 256 s each, resulting in 150 intervals for observation 002 and 173 intervals for observation 004. For each of these intervals, we produced a cospectrum, and then averaged these cospectra together. The frequencies sampled are limited to the range 256^{-1} Hz $< \nu <$ 256 Hz. The low end of this range is determined by the interval length, and the high end is determined by the sampling rate of the light curves. The resulting averaged, rms-normalized cospectra for observations 002 and 004 are shown in black in Figure 7, where they have been rebinned for clarity. Their corresponding best-fit models, described below, are shown in the same figure in red. All errors quoted are 1-σ.

4.1.2. Modeling the Power Spectra

Similar to our analysis in Section 3.1, we fit the cospectra with a model consisting of a sum of Lorentzian functions following Belloni et al. (2002).

We used an automated modelling algorithm which fits a cospectrum to composite Lorentzian models with progressively more components, halting when the addition of a component no longer results in the reduction of the χ^2 fit statistic. We chose the model with the minimum number of components which still resulted in a significant improvement to the fit ($|\Delta\chi^2| > 10$), and discard more complex models with only marginally better fit statistics. For observation 002, this results in a single-component model containing only one broad Lorentzian with unconstrained ν_0 and Q. For observation 004, we obtain a model with two broad components centered at considerably higher frequencies than that of the component obtained for observation 002. Following the notation of Klein-Wolt & van der Klis (2008), we dub the lowest frequency broad components L_b, and the higher frequency broad component observed in observation 004, L_h.

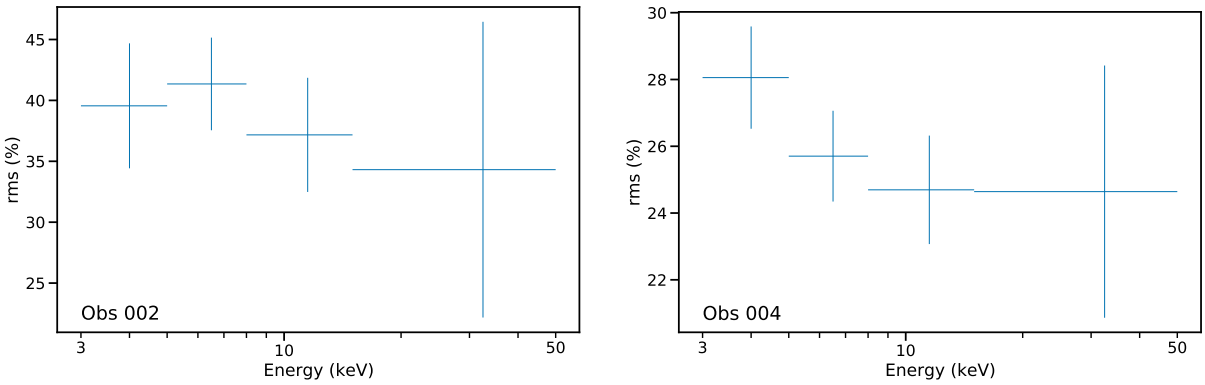

Figure 8. The observed variability as measured by the fractional rms is shown as a function of photon energy for observation 002 on the left and 004 on the right. While observation 002 is consistent with a flat rms-energy relation, observation 004 shows evidence of decreasing variability with increasing energy.

Table 5. *NuSTAR* power spectral components.

OBSID	Component	$\nu_{\max}$ (Hz)	Q	rms (%)
90601315002	L_b	$0.05^{\dagger}$	$3 \times 10^{-4\,\dagger}$	54 ± 5
90601315004	L_b	0.5 ± 0.1	0.15 ± 0.03	28 ± 1
	L_h	5.7 ± 1.4	0.9 ± 0.6	14 ± 3
	$L_{\rm LF}$	2.3 ± 0.1	2.6 ± 1.0	9.5 ± 1.9

† The characteristic frequency and quality factor are not constrained for observation 002, therefore errors are not shown for these quantities.

Following the detection of the two broad components in observation 004 using our fitting algorithm, visual inspection suggested the presence of an additional component at ~ 2 Hz. We therefore added a third QPO-like component to the model and saw a small but significant improvement to the fit of $\Delta\chi^2 = -30$. We label this narrower QPO-like component $L_{\rm LF}$. We calculate the significance of this component to be 2.5σ. Here we define the significance as the ratio of the integrated power of the component to its error, A/σ_A. Note that this component lines up with the QPO seen in the *NICER* PDS (panel b of Figure 6), and it is therefore still significant. All of the components observed in each observation as well as their fitted parameters are listed in Table 5. The components and the resulting composite models are shown in red in Figure 7.

4.1.3. Determining the rms-energy relation

Finally, in order to better understand the physical origins of the source variability, we computed the variability as a function of photon energy for each observation. For four energy ranges, we produced cospectra using the same method described in Section 4.1.1. For each energy range, we filtered events accordingly, and we again binned the light curves with a time resolution of 512^{-1} s and produced cospectra for intervals of 256 s which were then averaged to produce a single cospectrum. By integrating the cospectra we are therefore able to determine the fractional rms. Due to the limited frequency range for which significant power is detected in each observation, we did not integrate over the entire available frequency range. Rather, for observation 002, we integrated the power between 256^{-1} Hz and 1 Hz, while for observation 004, we integrated the power between 256^{-1} Hz and 10 Hz. The resulting rms-energy relations are shown in Figure 8. Observation 002 is consistent with a flat rms-energy relation, whereas observation 004 may exhibit decreasing variability with increasing photon energy. The latter result indicates that cooler regions of the source are more variable than hotter regions, perhaps due to inhomogeneities in an accretion disk.

4.2. Pulsation Search

4.2.1. Clock-correction

The time stamp for *NuSTAR* is accurate up to 100 μs (Bachetti et al. 2020). This improvement can be attributed to a recent finding that the frequency response of the time reference temperature-compensated quartz oscillator aboard *NuSTAR* is dependent on time and temperature.The clockfiles can be generated with `nustar-clock-utils`[5]. We used the clockfile, `v108`, released with *NuSTAR* CALDB version 20200813 and apply it to the event files using `barycorr`. This clock file not only applies the correction mentioned above but also the 5-ms absolute time shift with respect to UTC as observed from cross-correlation with *NICER*.

[5] See https://github.com/nustar/nustar-clock-utils

4.2.2. Temporal Variability

After applying the clock corrections we used HENDRICS, a software package as part of Stingray (Huppenkothen et al. 2019), to perform the timing analysis. Initially developed as MaLTPyNT (Bachetti 2015) for timing analysis of *NuSTAR* data, HENDRICS now comprises of tools such as acceleration searches (Ransom et al. 2002), periodograms, Z_n^2 statistics to search for pulsations and extends to some other X-ray missions (e.g., *NICER*).

We began this analysis by first calibrating the datafile by using the response file for each observation and constructing the lightcurve using HENcalibrate. The intent here was to check if AT2019wey shows rapid variability along with modality such that the lightcurve can be distributed into 'high', 'low' and 'flare' regions as seen in transitional millisecond pulsars. No modality was observed.

4.2.3. Pulse Search

Similar to the techniques used in Section 3.2.1, we launched acceleration search using PRESTO to search for periodic pulsations. Fourier domain search techniques allow for mitigation of Fourier power spread over frequency bins due to binary motion in short period orbital binaries. We split the observation into chunks of 720 s each and allowed for 5% overlap within these chunks. We then used HENbinary from Hendrics to render these time series in the format preferred by accelsearch. Simultaneoulsy, we binned the lightcurve to 1 ms bins. After that, we used the accelsearch routine in PRESTO and searched to a depth of zmax of 10 and detection threshold of 2σ. No viable "candidates" were detected.

5. *NuSTAR-NICER-Chandra-Swift*/XRT Spectral Analysis

In this Section, we perform joint spectral analysis of three sets of simultaneous observations obtained in April, on 16 August, and 20 September 2020. All spectral fitting is performed using XSPEC version 12.11.0 (Arnaud 1996). During the April 2020 epoch, the *NuSTAR* 002 spectra for FPMA and FPMB (Table 2) were simultaneously fit along with data from all four *Swift*/XRT observations obtained in April 2020 (Table 3). For the August 2020 epoch the *NuSTAR* 004 spectra for FPMA and FPMB (Table 2) were simultaneously fit along with two *NICER* observations bracketing the *NuSTAR* observation (Table 1, obsID 3201710112 and 3201710113). For the September 2020 epoch the *Chandra* spectra were simultaneously fit along with two *NICER* observations bracketing the *Chandra* observation (Table 1, obsID 3201710147 and 3201710148).

5.1. Data Reduction

5.1.1. NuSTAR

To generate the spectra for FPMA and FPMB, source photons were extracted from a circular region with a radius of 60″ centered on the apparent position of the source in both FPMA and FPMB. For 002 the background was extracted from a 100″ region located on the same detector, while for 004 the source was bright enough that a smaller portion of the field-of-view could be used to estimate the background, so the background was extracted from a 60″ region.

5.1.2. NICER

We generate GTIs using nimaketime to select events that occurred when the particle background was low (KP $<$ 5 and COR_SAX $>$ 4), while avoiding times of extreme optical light loading (FPM_UNDERONLY_COUNT $<$ 200) and low Sun angle (SUN_ANGLE>60). Using niextract-events, the GTIs were applied to the data selecting EVENT_FLAGS=bxxx1x000 and PI energy channels between 25 and 1200, inclusive. For more information on the *NICER* screening flags, see Bogdanov et al. (2019). The resulting event files were loaded into XSELECT to extract a combined spectrum with an exposure time of 5.7 ks after filtering. Systematic errors of 1% in the $2-10$ keV band and 5% in the $0.3-2$ keV band were added to the *NICER* spectrum via grppha.

A background spectrum was generated using the nibackgen3C50 tool for each cleaned event file and ufa event file pair. These were then combined into a single background spectrum that was weighted by the duration of each observation. We use the standard public RMF and the on-axis average ARF available in CALDB release 20200722 when modeling the NICER spectrum.

5.1.3. Chandra

Plus and minus first-order ($m = \pm 1$) MEG and HEG data were extracted from the -1 and the $+1$ arms of the MEG and HEG gratings for the source and the background, using the CIAO tool tgextract. CIAO version 4.12.1 and the associated caldb version 4.9.3 were used in the analysis. Spectral redistribution matrix files and effective area files were generated with mkgrmf and mkgarf.

5.1.4. Swift/XRT

We reduce the *Swift*/XRT data using xrtproducts in HEAsoft version 6.27.2, adopting a 50″ radius circular region around the known position, and a 100″ radius, circular, source-free background region.

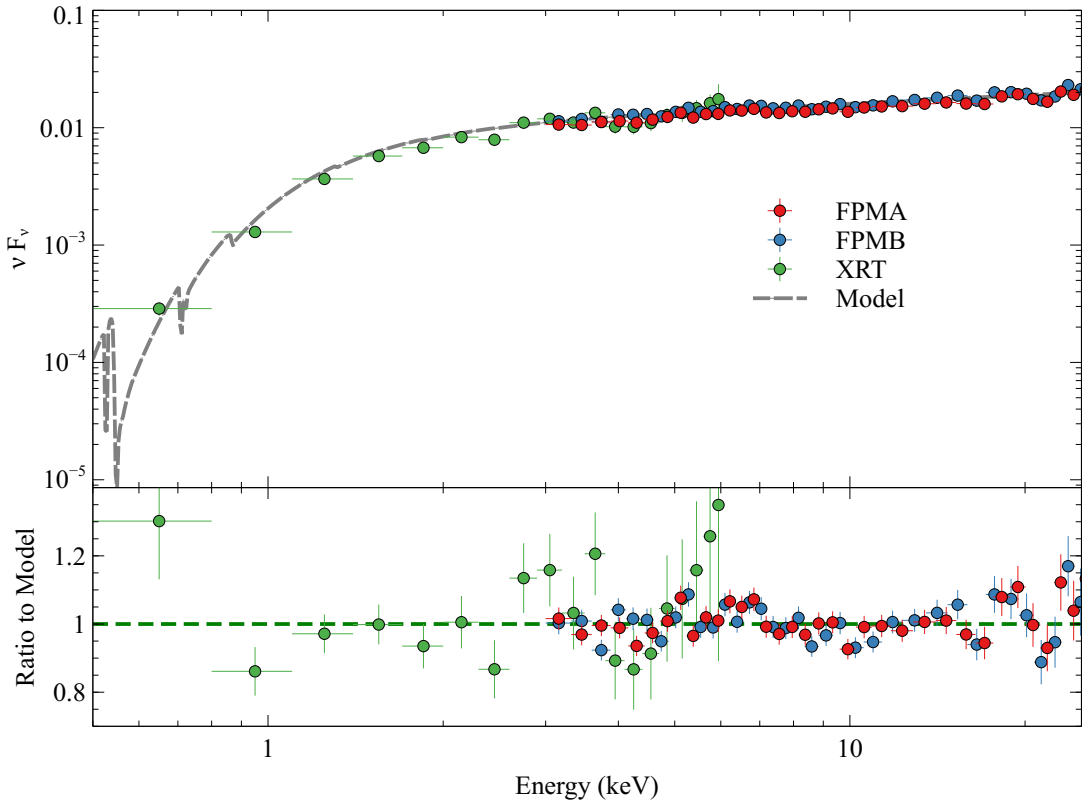

Figure 9. *Top* Unfolded spectrum of the data from the two *NuSTAR* telescopes and the combined *Swift*-XRT data. The best-fit model for *NuSTAR*-FPMA is shown for comparison. *Bottom* The ratio to the best-fit model is shown for all three data sets. The data have been rebinned for visual clarity.

5.2. Joint spectroscopic analysis

5.2.1. April, 2020

Table 6. April, 2020 Spectroscopic Fits

Parameter	90% Interval
`constant`	
$\mathcal{C}_{\rm FPMA}$	1 (frozen)
$\mathcal{C}_{\rm FPMB}$	1.081 ± 0.009
$\mathcal{C}_{\rm XRT}$	0.825 ± 0.025
`tbabs`	
$N_{\rm H}$ (10^{22} cm^{-2})	0.60 ± 0.03
`powerlaw`	
Γ	1.76 ± 0.01
`norm`†	8.65 ± 0.15
`W-stat / d.o.f.`	4277/4039

†: normalization at 1 keV in units of 10^{-3} ph keV^{-1} cm^{-2}.

The spectrum appears relatively featureless during this epoch (Figure 9) and can be adequately described by an absorbed power-law (`tbabs*powerlaw`, in XSPEC, Wilms et al. 2000). We also included a leading cross-calibration term (`constant`; Madsen et al. 2017) between the two *NuSTAR* telescopes (with FPMA defined to be 1) and a single term used for all four *Swift*/XRT observations. All data were fit using W-statistics via `cstat` (Cash 1979) on the un-binned data in both *NuSTAR* and *Swift*. For *NuSTAR* we fit the data over the 3–40 keV range as the source spectrum becomes comparable to the background at higher energies, while for *Swift* we fit from 0.5 to 6 keV.

To estimate the confidence intervals for the parameters we utilized the EMCEE (Foreman-Mackey 2013) implementation in XSPEC to explore the parameter space. We use 20 walkers with a chain length of 2×10^5 iterations and ignored the first 2×10^4 iterations to allow the fit to "burn in" and after which the solution had converged. We estimated 90% confidence intervals using `corner` (Foreman-Mackey 2016). The best fit values and the estimated confidence intervals are given in Table 6. We do note that the cross-normalization term for *Swift*/XRT is lower than we would typically expect. However, as the source count rate is relatively high for XRT (0.6 count s^{-1}, Table 3), a probable cause here is some pulse pile-up resulting in a lower-than-expected observed flux.

The unabsorbed flux in the 0.3–100 keV band for FPMA is $\sim 1.0 \times 10^{-10}\,\mathrm{erg\,cm^{-2}\,s^{-1}}$ ($\sim$1.2 mCrab). Paper II constrains the distance of AT2019wey to be $1 \lesssim D \lesssim 10$ kpc. At distances of [1, 3, 5, 10] kpc, this corresponds to a luminosity of [0.1, 1.1, 3.1, 12.5]$\times 10^{35}\,\mathrm{erg\,s^{-1}}$. The Eddington luminosity is $L_{\rm Edd} = 1.46 \times 10^{38} (M/M_\odot)\,\mathrm{erg\,s^{-1}}$ (assuming solar hydrogen mass fraction $X = 0.71$). Therefore, the X-ray luminosity in April 2020 is $10^{-5} \lesssim L_{\rm X}/L_{\rm Edd} \lesssim 10^{-3}$ for a $\approx 10\,M_\odot$ compact object.

5.2.2. August, 2020

The upper panel of Figure 10 shows the spectrum in the *NuSTAR* 004 data and simultaneous *NICER* observation, where the inset presents the ratio of data to an absorbed power-law model (`tbabs*powerlaw`) fitted only to the 3–4 keV and 10–12 keV energy bands ($\Gamma \sim 1.8$). As reported by Yao et al. (2020a), we clearly detected broadened Fe line and Compton hump, characteristic of the reflection spectrum commonly seen in accreting X-ray binaries (García et al. 2011). The spectrum can be described by a combination of disk black body and relativistic reflection from an accretion disk (`tbfeo*edge*(simplcutx*diskbb+relxillCp)`, in XSPEC). In this model, the continuum is assumed to be produced by Comptonization of the disk photons (`simplcut*diskbb`, Steiner et al. 2017; Mitsuda et al. 1984), and the reflection is fitted with a `relxill` model (García et al. 2014; Dauser et al. 2014) that incorporates such continuum (`relxillCp`). A photoelectric absorption `edge` is added to account for instrumental uncertainties within the spectrum where *NICER*'s calibration is still ongoing (see, e.g., Ludlam et al. 2020)

In the `relxillCp` model, the Γ parameter (power law index of the incident spectrum) is fixed at the same value as that in the `simpcutx` model. The black hole spin parameter (a) is fixed at 0. The inner emissivity index ($q_{\rm in}$) and outer emissivity index ($q_{\rm out}$) are frozen at 3 throughout the accretion disk, making $R_{\rm break}$ obsolete. The outer disk radius ($R_{\rm out}$) is fixed at $400\,r_{\rm g}$, where $r_{\rm g} = GM/c^2$ is the gravitational radius. The cutoff energy kT_e is fixed at 1 MeV. The reflection fraction $R_{\rm F}$ in the `simplcutx` and `relxillCp` models are fixed at 1. Redshift (z) is fixed at 0 since AT2019wey is a Galactic source. Similar to Section 5.2.1, we include a cross-normalization term (`constant`) between FPMA, FPMB, and *NICER* data. Other parameters include scattering fraction ($f_{\rm sc}$), inclination of the system (i), inner disk radius ($R_{\rm in}$) in units of the innermost stable circular orbit (ISCO), ionization parameter ($\log\xi$), iron abundance ($A_{\rm Fe}$), and a normalization parameter ($\mathrm{Norm_{rel}}$).

Table 7. August 16, 2020 Spectroscopic Fits

Parameter	90% Interval
`constant`	
$\mathcal{C}_{\rm FPMA}$	1 (frozen)
$\mathcal{C}_{\rm FPMB}$	1.051 ± 0.003
$\mathcal{C}_{NICER}$	1.035 ± 0.002
`tbfeo`	
$N_{\rm H}$ (10^{22} cm^{-2})	0.513 ± 0.003
O	< 0.020
Fe	< 0.0528
z	0 (frozen)
`simplcutx`	
Γ	1.786 ± 0.001
$f_{\rm sc}$	0.746 ± 0.005
$R_{\rm F}$	1 (frozen)
kT_e (keV)	1000 (frozen)
`diskbb`	
$T_{\rm disk}$ (keV)	0.3542 ± 0.0001
$\mathrm{R_{in}^{*}}$ †	40.58 ± 0.03
`relxillCp`	
$q_{\rm in} = q_{\rm out}$	3 (frozen)
$R_{\rm break}$ ($R_{\rm isco}$)	1 (frozen)
a	0 (frozen)
i (deg)	$27.0^{+0.8}_{-1.2}$
$R_{\rm in}$ ($R_{\rm isco}$)	< 1.05
$R_{\rm out}$ ($R_{\rm g}$)	400 (frozen)
$\log\xi$	$3.0121^{+0.0016}_{-0.0020}$
$A_{\rm Fe}$	$2.86^{+0.10}_{-0.09}$
kT_e (keV)	1000 (frozen)
$R_{\rm F}$	1 (frozen)
$\mathrm{Norm_{rel}}$ (10^{-4})	2.96 ± 0.03
`edge`	
$E_{\rm c}$ (keV)	$1.369^{+0.017}_{-0.016}$
D	$0.071^{+0.005}_{-0.005}$
`C-stat / d.o.f.`	2006.52 (1769)

†: normalization $(R_{\rm in}/D_{10})\sqrt{\cos i}$, where $R_{\rm in}$ is the inner disk radius in the unit of km, and D_{10} is distance to the source in units of 10 kpc.

The *NuSTAR* data are groupped to have signal-to-noise ratio $SNR = 6$ and oversample of 3. All data were fit using C-statistics via `cstat` (Cash 1979). For *NuSTAR* we fit the data over the 3–79 keV range, while for *NICER* we fit from 0.8 to 10 keV. The best fit values and the estimated confidence intervals are given in Table 7. In the particular fit, we frozen a few parameters at fixed values to reduce the complexity of this model.

We experienced by setting the maximum spin $a = 0.998$:

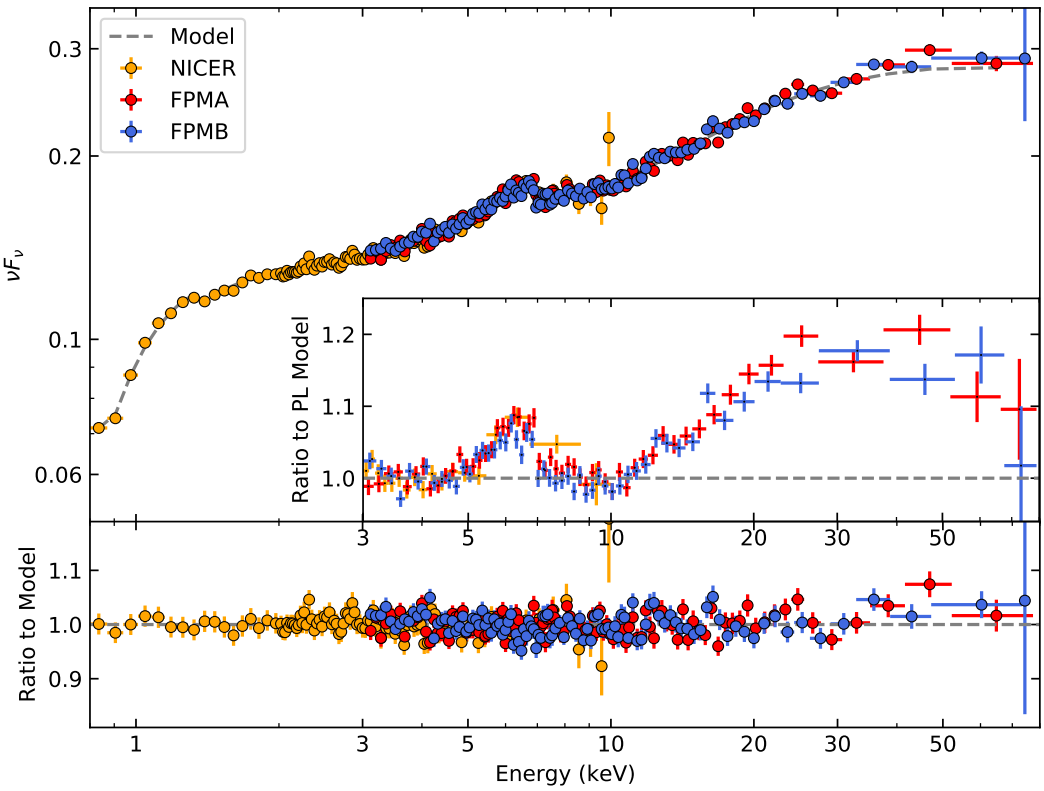

Figure 10. *Top*: Unfolded spectrum of the data from the two *NuSTAR* telescopes and the combined *NICER* data. The best-fit model for *NuSTAR*-FPMA is shown for comparison. The inset shows the ratio to a simple power-law fitted only to the 3–4 keV and 10–12 keV energy ranges to emphasize features in the reflection spectrum. *Bottom*: The ratio to the best-fit model. The data have been rebinned for visual clarity.

- If we let $R_{\rm in}$, q, and i be free, then the fitting resulted in parameters loosely constrained, as most of these are correlated.

- If we fix the inclination to the value obtained in the previous fit ($i = 27.0°$), and allow $R_{\rm in}$ and q to be free, then the fitting improves, with similar statistics to that with $a = 0$ (Table 7). However, this model results in a flatter emissivity law ($q \sim 2.8$) with an inner radius still relatively close to ISCO ($R_{\rm in} \sim 4 \pm 3\, R_{\rm ISCO}$). This is contrary to the theoretical expectation of a steep emissivity profile for rapidly rotating black holes with compact coronae, unless the source of power-law photons is placed much farther along the rotational axis, which conversely will result in weaker reflection features (see Fig. 3 in Dauser et al. 2013).

- If we fix the inclination i to higher values (45°, 60°), then the fit quality decreases, with clear residuals around the Fe line. Therefore, from the point of view of reflection, the inclination (i) of the inner disk is well constrained.

The reflection spectrum is similar to those observed in other black hole binaries, such as GX 339−4 (Wang-Ji et al. 2018) or XTE J1550−564 (Connors et al. 2020). The unabsorbed flux in the 0.3–100 keV band for FPMA is $\sim 1.7 \times 10^{-9}$erg cm^{-2} s^{-1} (∼20 mCrab). At distances of [1, 3, 5, 10] kpc, this corresponds to a luminosity of $[0.2,\ 1.8,\ 5.1,\ 20.4] \times 10^{36}$ erg s^{-1}. Therefore, the X-ray luminosity on 16 August 202 is $1.4 \times 10^{-4} \lesssim L_{\rm X}/L_{\rm Edd} \lesssim 1.4 \times 10^{-2}$ for a 10 $M_\odot$ compact object.

5.2.3. September 20, 2020

The upper panel of Figure 11 shows simultaneous *Chandra* and *NICER* observations. To model the continuum, we adopted the `constant*tbabs*(simpl*diskbb+gaussian)` model, where `simpl` is a Comptonization model that generates the power-law component via Compton scattering of a fraction ($f_{\rm sc}$) of input seed photons from the disk (Steiner et al. 2009). The flag $R_{\rm up}$ was set to 1 to only include upscattering. The `gaussian` component is added to account for the existence of a relativistic broadened iron line, and we fix the line center ($E_{\rm line}$) at 6.4 keV. We fit the *NICER* data over the 2.5–9.0 keV

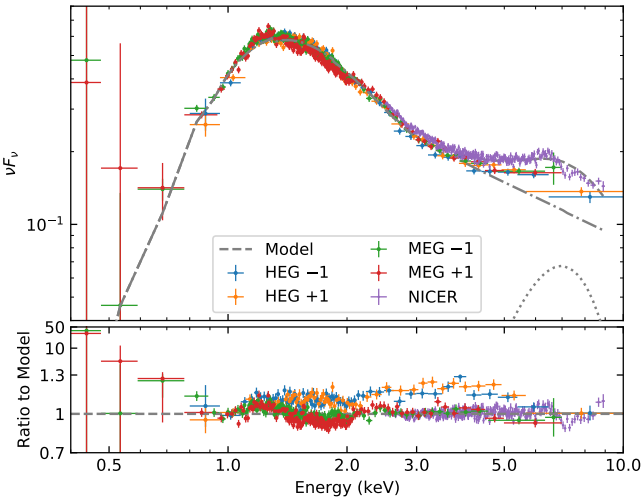

Figure 11. *Top*: Unfolded spectrum of the data from *Chandra*/HETG and the combined *NICER* data. For comparison, we show the best-fit model for *NICER* above 4.0 keV and the best-fit model for MEG −1 below 4.0 keV. *Bottom*: The ratio to the best-fit model is shown for all three data sets. The y-axis is shown in linear scale from 0.7 to 1.3, and in log scale from 1.3 to 50. The data have been rebinned for visual clarity.

Table 8. September 20, 2020 Spectroscopic Fits

Parameter	90% Interval
`constant`	
$\mathcal{C}_{\rm HETG}$	1 (frozen)
$\mathcal{C}_{NICER}$	0.901 ± 0.007
`tbabs`	
$N_{\rm H}$ (10^{22} cm^{-2})	$0.417^{+0.014}_{-0.013}$
`simpl`	
Γ	2.80 ± 0.05
$f_{\rm sc}$	0.176 ± 0.007
$R_{\rm up}$	1 (fixed)
`diskbb`	
$T_{\rm disk}$ (keV)	$0.315^{+0.004}_{-0.005}$
$R^*_{\rm in}$ †	136 ± 6
`gaussian`	
$E_{\rm line}$ (keV)	6.4 (fixed)
$\sigma_{\rm line}$ (keV)	1.84 ± 0.09
Norm$_{\rm line}$ ‡	0.0074 ± 0.0007
χ^2 / `d.o.f.`	12095.94 (23735)

†: $R^*_{\rm in}$ has the same meaning as that in Table 7.
‡: Normalization of the Gaussian in photon cm^{-2} s^{-1}.

range. For HEG and MEG, we include the 0.8–10 keV and 0.4–7.0 keV bands, respectively. All data were fit using χ^2-statistics. The best fit values and the estimated confidence intervals are given in Table 8. The best-fit model is over-plotted with the unfolded spectrum in Figure 11.

As can be seen from the bottom panel of Figure 11, the model under-predicts the MEG data below ~ 0.8 keV. The MEG effective area below 1 keV is sensitive to the correction for contamination, which currently undercorrects for the increasing depth of the contaminant. The magnitude of the effect is estimated to be about 20% at 0.65 keV and 10% at 0.8 keV, in the sense that estimated MEG fluxes should be even larger than shown in Figure 11. The excess in the very soft X-ray band might arise from reprocessing of X-rays in the outer accretion disk. Paper II shows that the bright UV/optical emission can be described with the `diskir` model (Gierliński et al. 2009) with a relatively large value of irradiation fraction $f_{\rm out} \sim 0.08$.

The HETGS data can be used to constrain $N_{\rm H}$. By fitting a simple model to a limited wavelength range, the Mg I and Ne I edges due to the ISM can be determined directly. The continuum model in this case is empirical, a log-parabolic shape, and the edge is modeled in `isis` using the `edge` model, which has no structure at the edge but has the appropriate asymptotic behavior for the ISM edge. Fitting the 11-17 Å region (0.73-1.13 keV) region, we find that the Ne I edge optical depth is $0.170^{+0.06}_{-0.07}$ (at 90% confidence), giving an estimate of $N_{\rm H}$ of $2.2^{+0.7}_{-0.9} \times 10^{21}$ cm^{-2} using the ISM model of Wilms et al. (2000). An optical depth at the Ne I edge of 0.33 is expected when $N_{\rm H} = 4.2 \times 10^{21}$ cm^{-2}, which is ruled out at the 4.3 σ level. An independent measurement from fitting the Mg I line in the 8-11 Å (1.13-1.55 keV) region gives an optical depth of $0.043^{+0.021}_{-0.014}$, and $N_{\rm H} = 3.1^{+1.5}_{-1.0} \times 10^{21}$ cm^{-2}. Taken together, the HETGS data indicate that $N_{\rm H}$ is about 2.5×10^{21} cm^{-2}, or about a factor of two smaller than derived from the continuum fit, given in Table 8. If the $N_{\rm H}$ due to the ISM is truly this low, then the soft excess could be considerably stronger and softer than indicated by the global fit.

6. *NICER* Spectral Analysis

To examine the source evolution during the X-ray brightening and outbursts (Figure 1), we analyze the *NICER* 0.8–10 keV energy spectrum for each OBSID between 3201710105 and 3201710157 (Table 1). We have adopted the same analysis methods for source and background spectrum along with systematic uncertainty as described in Section 5.1.2. Each spectrum is grouped into channels by considering a minimum of 32 counts per channel bin.

The energy spectrum is first fitted by an absorbed power-law model. However, this fails to describe the continuum of AT2019wey due to residuals observed in

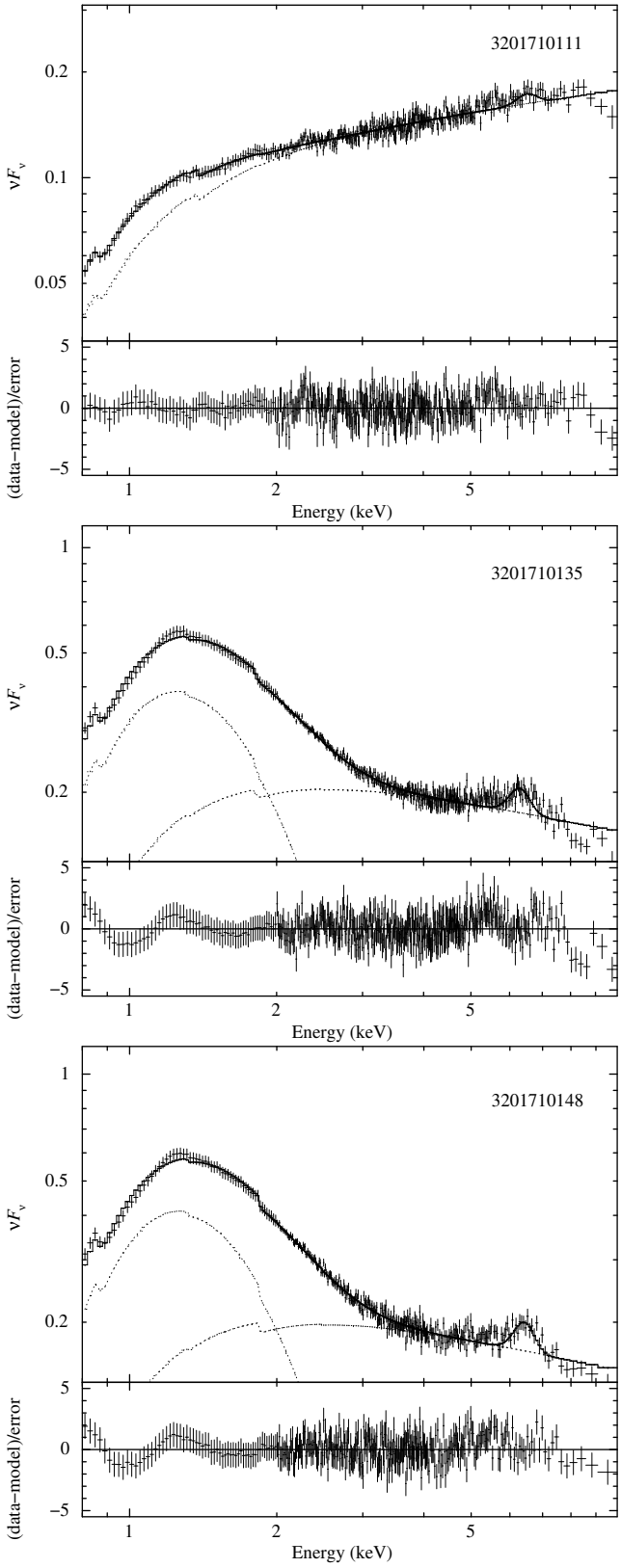

Figure 12. *NICER* spectral fitting at three representative epochs, OBSID 3201710111, 3201710135, and 3201710148.

the soft X-rays. Adding a multi-blackbody component `diskbb` at this stage leads to an acceptable fit. We also included a ≈1.4 keV edge feature in the model, as found to be present in the *NICER* and *NuSTAR* broadband analysis (Table 7). Similar to the broadband analysis (Section 5.2.2), the absorption component was described by `tbfeo` component. The only difference is that we fixed O & Fe to the Solar composition. The best-fitted model provides a reduced-χ^2 close to 1 in most of the cases. Some of the observations at brighter epochs includes a signature of the iron fluorescence line. Adding a Gaussian line component at 6.3–6.5 keV improves the fitting further, while the line width is not well constrained due to the weak nature of the line in *NICER* data. A final version of the model in XSPEC hereafter reads as: `tbfeo*(diskbb+pegpwrlw+gaussian)*edge`. The model fitting at three representative epochs (59076, 59100, and 59113 MJD) are shown in Figure 12.

The evolution of spectral parameters such as equivalent hydrogen column density N_H in 10^{22} cm^{-2}, power-law photon index Γ, temperature at inner disk radius T_{disk} in keV, and the disk-blackbody normalization term $Norm_{disk} = (R_{in}/D_{10})^2 cos i$ are shown in Figure 13. In the bottom panel of Figure 13, we present the unabsorbed 0.4–10 keV fluxes in the disk-blackbody component, the power-law component, and the total (disk-blackbody + power-law + Gaussian). Note that the line flux is significantly smaller than the other two components. Among the fitted parameters, the column density varies in a range of $(0.30–0.55) \times 10^{22}$ cm^{-2}. The photon index gets softer, from 1.7 to 2.3, when AT2019wey reaches peak of the outbursts (≈59112 MJD), and gets harder again afterwards. The inner disk temperature at the same time stays almost constant at ∼0.32 keV with an evolving disk blackbody normalization especially at outburst maxima. Furthermore, thermal and non-thermal fluxes from disk-blackbody and power-law components follow an interesting pattern, respectively. The non-thermal flux gradually changes over the outburst. However, the thermal flux coincides with sudden episodic enhancements observed in the outburst light curve at several epochs.

Note that the apparent N_H variation shown in the top panel of Figure 13 is likely a modelling systematic. This is an expected issue that is driven by Γ, which can be readily see in the top two panels of Figure 13. Paper II measured the equivalent width (*EW*) of Na I D line and diffuse interstellar bands (DIBs) from optical spectra obtained in March, July, and September 2020. The measured *EW* does not exhibit significant variability. In that paper we constrain the line-of-light extinction toward AT2019wey to

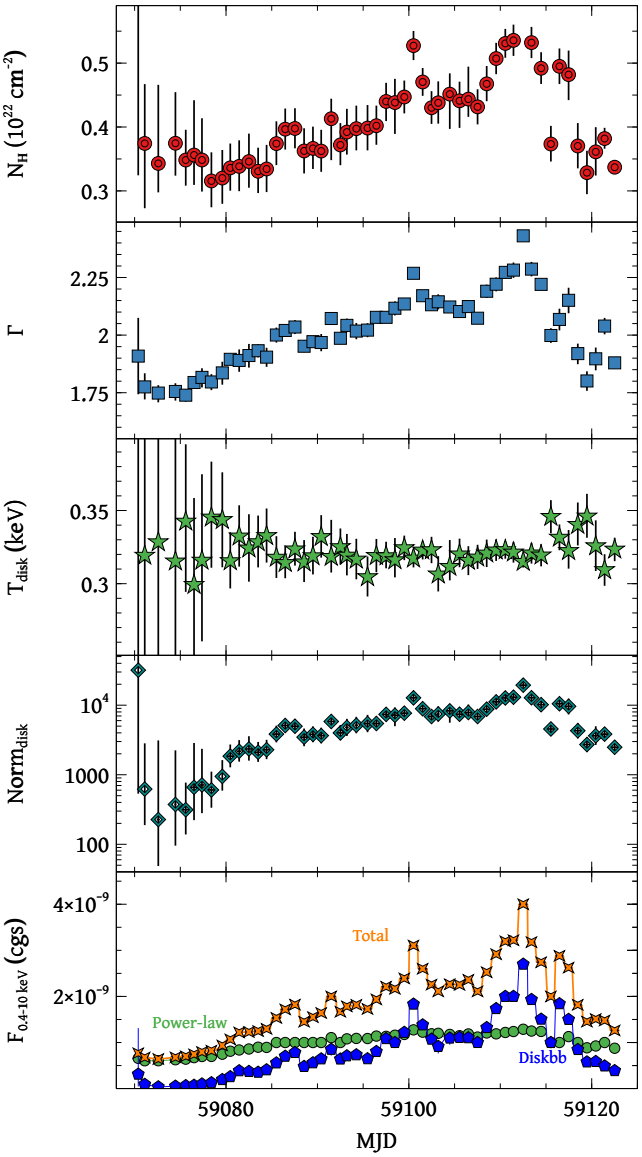

Figure 13. Evolution of *NICER* spectral best-fit parameters, and unabsorbed 0.4–10 keV flux from the `diskbb` component (blue pentagons), the `pegpwrlw` component (green circles), and the total (orange crosses). The error on spectral parameters is estimated for a 90% confidence level.

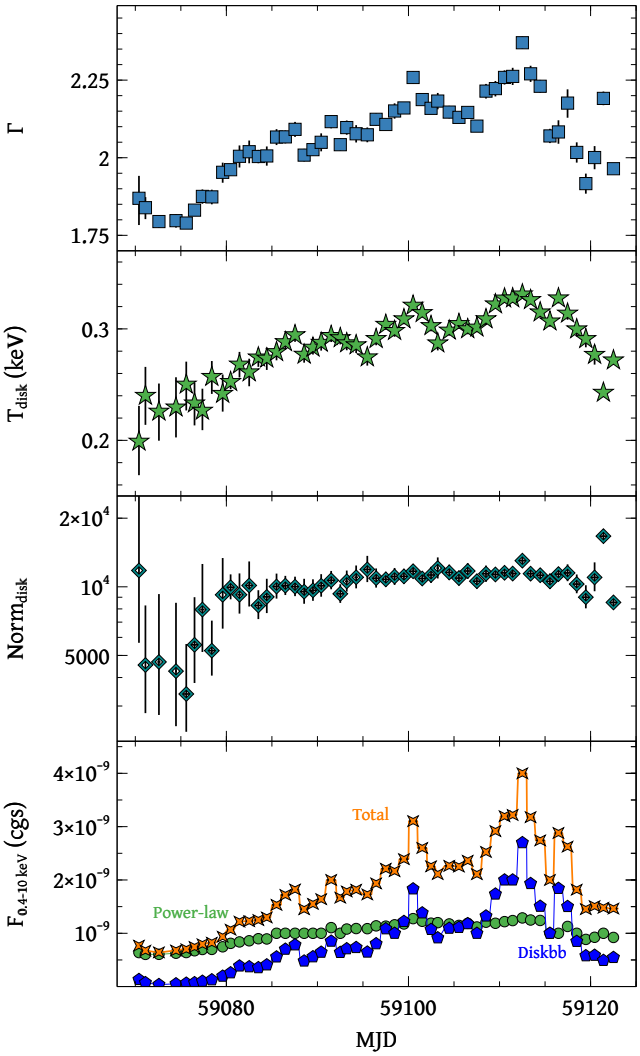

Figure 14. Same as Figure 13, but fixing $N_{\rm H} = 5 \times 10^{21}\,{\rm cm}^{-2}$ in the model fitting.

be 0.8 mag $\lesssim E(B-V) \lesssim$ 1.2 mag. Using the calibration of $N_{\rm H} = 5.55 \times 10^{21} \times E(B-V)$ (Predehl & Schmitt 1995), the line-of-sight column density to AT2019wey can be inferred to be $4.4 < N_{\rm H}/(10^{21}\,{\rm cm}^{-2}) < 6.7$.

In order to investigate how the column density variation affects the derived parameters, we also fit the *NICER* spectra adopting the same model by fixing $N_{\rm H} = 5.0 \times 10^{21}\,{\rm cm}^{-2}$. The resulting evolution of model parameters is shown in Figure 14. The major difference lies in the disk parameters. In Figure 13, $T_{\rm disk}$ is almost constant across the burst. However, after fixing $N_{\rm H}$ in the latter case, $T_{\rm disk}$ shows quite a remarkable evolution with an almost constant disk normalization parameter after a certain epoch ($\gtrsim$ 59082 MJD). This provides evidence that the inner disk radius ($R_{\rm in}$) remained at $\sim$ 100–1000 km assuming a range of distance from $D \sim 10$ kpc to 1 kpc (Paper II). One can expect the change in the disk-blackbody (soft component) as the column density is fixed. The most interesting aspect is whatever criteria we adopt the disk-blackbody flux matches the occasional enhancement observed in the source light curve. The power-law component is free from the choice of the adopted method.

7. Conclusions

7.1. Spectral-Timing Properties

In this paper we have presented comprehensive pre-discovery and follow up X-ray observations of the Galac-

tic transient AT2019wey. The X-ray spectral-timing properties of AT2019wey is entirely in line with typical properties of the low/hard state (LHS) and hard-intermediate state (HIMS) LMXBs. Paper II infers that the compact object is probably a BH based on the bright optical luminosity. The classification scheme of different accretion states of BH LMXBs has been outlined in, e.g., Fender et al. 2004; Remillard & McClintock 2006; Done et al. 2007; Belloni 2010.

(a) Before 59082 MJD (Aug 21), AT2019wey exhibits a hard spectrum ($1.7 \lesssim \Gamma \lesssim 2.0$) with little contribution from the disk component (Figure 14). The spectrum softens as the source brightens. It moves along the HL on the RID as the fractional rms stays at 30%. No QPO was observed (Section 3.1). The source stays in the canonical LHS of LMXBs.

(b) Between 59082 MJD and 59120 MJD (Sep 28), the PL component steepens ($2.0 \lesssim \Gamma \lesssim 2.3$), and the thermal disk emission becomes comparable or exceeds to the PL component in the 0.4–10 keV band (Figure 14). At the same time, the source leaves the HL on the RID as the fraction rms decreases. Low-frequency type-C QPO was observed, and its characteristic frequency increases as the disk flux increases. These properties indicate that AT2019wey enters into the canonical hard-intermediate state (HIMS).

The transition from LHS to the HIMS is smooth. It is not clear if the AT2019wey goes back to the LHS or still remains in the HIMS after > 59120 MJD. We are undertaking continued *NICER* observations of AT2019wey to monitor it in the X-ray. We note, however, that after being X-ray active for at least $\sim$ 10 months, AT2019wey has not transitioned to the soft intermediate state (SIMS) or the high/soft state (HSS).

The X-ray properties observed in AT2019wey thus far makes it a promising candidate for the population of "hard-only" outbursts that never reach the HSS or thermal state, which constitute $\sim 40\%$ of the outbursts from known Galactic BH X-ray binaries (Tetarenko et al. 2016). The distance of this system is poorly constrained to $\sim$1–10 kpc (Paper II). Given the brightness of AT2019wey in the optical ($r \approx 17.4$ mag), the *Gaia* mission will be able to determine the parallax to the source and thus settle the distance. Assuming a typical distance at 3–5 kpc, the X-ray luminosity of AT2019wey remained at a few times $10^{35}\,\mathrm{erg\,s^{-1}}$ for $\sim$ 6 months in the LHS, increased by a factor of $\sim$ 10 to a few times $10^{36}\,\mathrm{erg\,s^{-1}}$ over $\sim$ 2 months, and stayed at this luminosity afterwards in the HIMS. This range of X-ray luminosity is at the lower end of the whole population of BH transients, but typical for "hard-only" outbursts. The orbital period of AT2019wey is constrained to be $P_{\rm orb} \lesssim 8$ hours, consistent with the expectation that systems with short orbital periods remain in the hard spectral states due to their low mass accretion rates (Meyer-Hofmeister 2004).

7.2. *The Intriguing Outburst Profile*

Brilliant outburst of LMXBs (also termed as X-ray novae) spans a wide range of morphological types (Chen et al. 1997). Theories for the canonical fast-rise exponential-decay profile of X-ray novae has been developed based on the disk-instability model (DIM), which has successfully reproduced dwarf novae outbursts (Lasota 2001). Disk truncation and irradiation are generally invoked to account for the longer evolution timescale and recurrence time of X-ray novae (van Paradijs 1996; Dubus et al. 2001). Recently, detailed analysis of the decay profile of X-ray outbursts provide evidence for the existence of generic outflows and time-varying irradiation (Tetarenko et al. 2018b,a).

The rise of AT2019wey's X-ray light curve is rather unique. Considering only outbursts from known BH LMXBs with short periods ($P_{\rm orb} \lesssim 5$ h), we find that light curves in the classical soft X-ray band either rise to maximum in 5–20 d as observed in MAXI J1659−152 (Kennea et al. 2011; Yamaoka et al. 2012; Kuulkers et al. 2013), XTE J1118+480 (Brocksopp et al. 2010), MAXI J1836−194 (Ferrigno et al. 2012), and Swift J1753.5−0127 (Shaw et al. 2013), or are already at the maximum upon discovery as observed in Swift J1357.2−0933 (Armas Padilla et al. 2013; Weng & Zhang 2015; Beri et al. 2019). However, for AT2019wey, the X-ray flux rose from $< 10\,\mu$Crab (2RXS upper limit) to $\sim$ 1 mCrab after the source being detected by optical surveys in early-December 2019 (Figure 3), remained at this level for nearly half a year, and only reached a maximum of $\sim$ 25 mCrab around mid-September 2020. The *MAXI* and *Swift*/BAT observations strongly rule out the existence of an X-ray nova-like outburst brighter than $\sim$ 5 mCrab before the major X-ray brightening started in June 2020. Interestingly, a fast-rise slow-decay outburst profile was observed in the optical (Paper II). New recipes in the DIM are needed to explain such an intriguing behaviour.

If the sensitivity of the X-ray all sky image goes fainter even by a factor of 3, we expect to see a large increase in sources similar to AT2019wey. This bodes well for *SRG* repeatedly looks at the sky.

Acknowledgments

YY thanks the Heising–Simons Foundation for support. RML acknowledges the support of NASA through Hubble Fellowship Program grant HST-HF2-51440.001. JAG acknowledges support from NASA grant 80NSSC17K0515 and from the Alexander von Humboldt Foundation. ZW acknowledges support from the NASA postdoctoral program.

This work was partially supported under NASA contract No. NNG08FD60C and made use of data from the *NuSTAR* mission, a project led by the California Institute of Technology, managed by the Jet Propulsion Laboratory, and funded by the National Aeronautics and Space Administration. We thank the *NuSTAR* Operations, Software, and Calibration teams for support with the execution and analysis of these observations. This research has made use of the *NuSTAR* Data Analysis Software (nustardas), jointly developed by the ASI Science Data Center (ASDC, Italy) and the California Institute of Technology (USA).

NICER research at NRL is supported by NASA.

References

Armas Padilla, M., Degenaar, N., Russell, D. M., & Wijnand s, R. 2013, MNRAS, 428, 3083
Arnaud, K. A. 1996, in Astronomical Society of the Pacific Conference Series, Vol. 101, Astronomical Data Analysis Software and Systems V, ed. G. H. Jacoby & J. Barnes, 17
Bachetti, M. 2015, MaLTPyNT: Quick look timing analysis for NuSTAR data, , , ascl:1502.021
Bachetti, M., Harrison, F. A., Cook, R., et al. 2015, ApJ, 800, 109
Bachetti, M., Markwardt, C. B., Grefenstette, B. W., et al. 2020, Timing Calibration of the NuSTAR X-ray Telescope, , , arXiv:2009.10347
Bartlett, M. S. 1948, Nature, 161, 686
Bellm, E. C., Kulkarni, S. R., Graham, M. J., et al. 2019, PASP, 131, 018002
Belloni, T. 2010, The Jet Paradigm, Vol. 794, doi:10.1007/978-3-540-76937-8
Belloni, T., & Hasinger, G. 1990, A&A, 227, L33
Belloni, T., Psaltis, D., & van der Klis, M. 2002, ApJ, 572, 392
Beri, A., Tetarenko, B. E., Bahramian, A., et al. 2019, MNRAS, 485, 3064
Bogdanov, S., Guillot, S., Ray, P. S., et al. 2019, ApJL, 887, L25
Boller, T., Freyberg, M. J., Trümper, J., et al. 2016, A&A, 588, A103
Brocksopp, C., Jonker, P. G., Maitra, D., et al. 2010, MNRAS, 404, 908
Burrows, D. N., Hill, J. E., Nousek, J. A., et al. 2005, SSRv, 120, 165
Canizares, C. R., Davis, J. E., Dewey, D., et al. 2005, PASP, 117, 1144
Casella, P., Belloni, T., & Stella, L. 2005, ApJ, 629, 403
Cash, W. 1979, ApJ, 228, 939
Chen, W., Shrader, C. R., & Livio, M. 1997, ApJ, 491, 312
Connors, R. M. T., García, J. A., Dauser, T., et al. 2020, ApJ, 892, 47
Dauser, T., Garcia, J., Parker, M. L., Fabian, A. C., & Wilms, J. 2014, MNRAS, 444, L100
Dauser, T., Garcia, J., Wilms, J., et al. 2013, MNRAS, 430, 1694
Done, C., Gierliński, M., & Kubota, A. 2007, A&A Rv, 15, 1
Dubus, G., Hameury, J. M., & Lasota, J. P. 2001, A&A, 373, 251
Evans, P. A., Beardmore, A. P., Page, K. L., et al. 2007, A&A, 469, 379
—. 2009, MNRAS, 397, 1177
Fender, R. P., Belloni, T. M., & Gallo, E. 2004, MNRAS, 355, 1105
Ferrigno, C., Bozzo, E., Del Santo, M., & Capitanio, F. 2012, A&A, 537, L7
Foreman-Mackey, D. 2013, Publications of the Astronomical Society of the Pacific, 125, 306
—. 2016, corner.py: Scatterplot matrices in Python, , , doi:10.21105/joss.00024
García, J., Kallman, T. R., & Mushotzky, R. F. 2011, ApJ, 731, 131
García, J., Dauser, T., Lohfink, A., et al. 2014, ApJ, 782, 76
Garmire, G. P., Bautz, M. W., Ford, P. G., Nousek, J. A., & Ricker, George R., J. 2003, in Society of Photo-Optical Instrumentation Engineers (SPIE) Conference Series, Vol. 4851, X-Ray and Gamma-Ray Telescopes and Instruments for Astronomy., ed. J. E. Truemper & H. D. Tananbaum, 28–44
Gehrels, N., Chincarini, G., Giommi, P., et al. 2004, ApJ, 611, 1005
Gendreau, K. C., Arzoumanian, Z., Adkins, P. W., et al. 2016, in Society of Photo-Optical Instrumentation Engineers (SPIE) Conference Series, Vol. 9905, Space Telescopes and Instrumentation 2016: Ultraviolet to Gamma Ray, 99051H
Gierliński, M., Done, C., & Page, K. 2009, MNRAS, 392, 1106
Graham, M. J., Kulkarni, S. R., Bellm, E. C., et al. 2019, arXiv e-prints, arXiv:1902.01945

Harrison, F. A., Craig, W. W., Christensen, F. E., et al. 2013, ApJ, 770, 103
Hori, T., Shidatsu, M., Ueda, Y., et al. 2018, ApJS, 235, 7
Huppenkothen, D., Bachetti, M., Stevens, A. L., et al. 2019, ApJ, 881, 39
Ingram, A. R., & Motta, S. E. 2019, NewAR, 85, 101524
Kennea, J. A., Romano, P., Mangano, V., et al. 2011, ApJ, 736, 22
Klein-Wolt, M., & van der Klis, M. 2008, ApJ, 675, 1407
Krimm, H. A., Holland, S. T., Corbet, R. H. D., et al. 2013, ApJS, 209, 14
Kuulkers, E., Kouveliotou, C., Belloni, T., et al. 2013, A&A, 552, A32
Lasota, J.-P. 2001, NewAR, 45, 449
Leahy, D. A., Darbro, W., Elsner, R. F., et al. 1983, ApJ, 266, 160
Ludlam, R. M., Cackett, E. M., García, J. A., et al. 2020, ApJ, 895, 45
Lyapin, A., Zaznobin, I., Khorungev, G., et al. 2020, The Astronomer's Telegram, 13576, 1
Madsen, K. K., Beardmore, A. P., Forster, K., et al. 2017, AJ, 153, 2
Markert, T. H., Canizares, C. R., Dewey, D., et al. 1994, in Society of Photo-Optical Instrumentation Engineers (SPIE) Conference Series, Vol. 2280, EUV, X-Ray, and Gamma-Ray Instrumentation for Astronomy V, ed. O. H. Siegmund & J. V. Vallerga, 168–180
Matsuoka, M., Kawasaki, K., Ueno, S., et al. 2009, PASJ, 61, 999
Mereminskiy, I., Medvedev, P., Semena, A., et al. 2020, The Astronomer's Telegram, 13571, 1
Merloni, A., Predehl, P., Becker, W., et al. 2012, arXiv e-prints, arXiv:1209.3114
Meyer-Hofmeister, E. 2004, A&A, 423, 321
Mihara, T., Nakajima, M., Sugizaki, M., et al. 2011, PASJ, 63, S623
Mitsuda, K., Inoue, H., Koyama, K., et al. 1984, PASJ, 36, 741
Morii, M., Yamaoka, H., Mihara, T., Matsuoka, M., & Kawai, N. 2016, PASJ, 68, S11
Motta, S., Muñoz-Darias, T., Casella, P., Belloni, T., & Homan, J. 2011, MNRAS, 418, 2292
Muñoz-Darias, T., Motta, S., & Belloni, T. M. 2011, MNRAS, 410, 679
Negoro, H., Nakajima, M., Aoki, M., et al. 2020, The Astronomer's Telegram, 13948, 1
Pavlinsky, M., Levin, V., Akimov, V., et al. 2018, in Society of Photo-Optical Instrumentation Engineers (SPIE) Conference Series, Vol. 10699, Proc. SPIE, 106991Y
Predehl, P., & Schmitt, J. H. M. M. 1995, A&A, 500, 459
Predehl, P., Andritschke, R., Arefiev, V., et al. 2020, arXiv e-prints, arXiv:2010.03477
Ransom, S. M., Eikenberry, S. S., & Middleditch, J. 2002, AJ, 124, 1788
Remillard, R. A., & McClintock, J. E. 2006, ARA&A, 44, 49
Shaw, A. W., Charles, P. A., Bird, A. J., et al. 2013, MNRAS, 433, 740
Steiner, J. F., García, J. A., Eikmann, W., et al. 2017, ApJ, 836, 119
Steiner, J. F., Narayan, R., McClintock, J. E., & Ebisawa, K. 2009, PASP, 121, 1279
Sugizaki, M., Mihara, T., Serino, M., et al. 2011, PASJ, 63, S635
Tetarenko, B. E., Dubus, G., Lasota, J. P., Heinke, C. O., & Sivakoff, G. R. 2018a, MNRAS, 480, 2
Tetarenko, B. E., Lasota, J. P., Heinke, C. O., Dubus, G., & Sivakoff, G. R. 2018b, Nature, 554, 69
Tetarenko, B. E., Sivakoff, G. R., Heinke, C. O., & Gladstone, J. C. 2016, ApJS, 222, 15
Tonry, J., Denneau, L., Heinze, A., et al. 2019, Transient Name Server Discovery Report, 2019-2553, 1
Tonry, J. L., Denneau, L., Heinze, A. N., et al. 2018, PASP, 130, 064505
van der Klis, M. 1988, in Timing Neutron Stars, Vol. 262, 27–70
van Paradijs, J. 1996, ApJL, 464, L139
Wang-Ji, J., García, J. A., Steiner, J. F., et al. 2018, ApJ, 855, 61
Weng, S.-S., & Zhang, S.-N. 2015, MNRAS, 447, 486
Wilkes, B., & Tucker, W., eds. 2019, The Chandra X-ray Observatory, 2514-3433 (IOP Publishing), doi:10.1088/2514-3433/ab43dc
Willingale, R., Starling, R. L. C., Beardmore, A. P., Tanvir, N. R., & O'Brien, P. T. 2013, MNRAS, 431, 394
Wilms, J., Allen, A., & McCray, R. 2000, ApJ, 542, 914
Yamaoka, K., Allured, R., Kaaret, P., et al. 2012, PASJ, 64, 32
Yao, Y., Garcia, J., Grefenstette, B., et al. 2020a, The Astronomer's Telegram, 13957, 1
Yao, Y., Enoto, T., Altamirano, D., et al. 2020b, The Astronomer's Telegram, 13932, 1
Zhang, L., Altamirano, D., Cúneo, V. A., et al. 2020a, MNRAS, 499, 851
Zhang, S.-N., Li, T., Lu, F., et al. 2020b, Science China Physics, Mechanics, and Astronomy, 63, 249502